Available online at www.sciencedirect.com
SCIENCE DIRECT
Tectonophysics 421 (2006) 1–22
TECTONOPHYSICS
www.elsevier.com/locate/tecto

Effect of water and stress on the lattice-preferred orientation of olivine

H. Jung [a,b,c,*], I. Katayama [b,1], Z. Jiang [b,2], T. Hiraga [c,3], S. Karato [b,4]

[a] School of Earth and Environmental Sciences, Seoul National University, Seoul 151-747, Republic of Korea
[b] Department of Geology and Geophysics, Yale University, New Haven, CT 06520, USA
[c] Department of Geology and Geophysics, University of Minnesota, Minneapolis, MN 55455, USA

Received 1 January 2005; received in revised form 21 February 2006; accepted 23 February 2006

Abstract

The influence of water and stress on the lattice-preferred orientation (LPO) of olivine aggregates was investigated through large strain, shear deformation experiments at high pressures and temperatures (P=0.5–2.1 GPa, T=1470–1570 K) under both water-poor and water-rich conditions. The specimens are hot-pressed synthetic olivine aggregates or single crystals of olivine. Water was supplied to the sample by decomposition of a mixture of talc and brucite. Deformation experiments were conducted up to γ (shear strain) ~ 6 using the Griggs apparatus where water fugacity was up to ~ 13 GPa at the pressure of 2 GPa. The water content in olivine saturated with water increases with increasing pressure and the solubility of water in olivine at P=0.5–2 GPa was ~ 400–1200 ppm H/Si. Several new types of LPO in olivine are found depending on water content and stress. Samples deformed in water-poor conditions show a conventional LPO of olivine where the olivine [100] axis is subparallel to the shear direction, the (010) plane subparallel to the shear plane (type-A). However, we identified three new types (type-B, C, and E) of LPO of olivine depending on the water content and stress. The type-B LPO of olivine which was found at relatively high stress and/or under moderate to high water content conditions is characterized by the olivine [001] axis subparallel to the shear direction, the (010) plane subparallel to the shear plane. The type-C LPO which was found at low stress and under water-rich conditions is characterized by the olivine [001] axis subparallel to the shear direction, the (100) plane subparallel to the shear plane. The type-E LPO which was found under low stress and moderate water content is characterized by the olivine [100] axis subparallel to the shear direction, the (001) plane subparallel to the shear plane. Observations by transmission electron microscopy (TEM) and scanning electron microscopy (SEM) show that the dislocations in water-poor samples (type-A) are curved and both **b**= [100] and **b**=[001] dislocations have a similar population. Numerous subgrains are seen in water-poor samples in backscattered electron images. In contrast, water-rich samples (both type-B and type-C) contain mostly **b**=[001] dislocations and dislocations are straight and sub-grain boundaries are rare compared to those in water-poor samples. These observations suggest that (1) dominant slip systems in olivine change with water fugacity (and stress) and (2) grain boundary migration is enhanced in the presence of water. Seismic anisotropy corresponding to the fabrics under water-rich condition is significantly different from that under water-poor condition. Consequently, the relationship between seismic anisotropy and flow geometry in water-rich regions is expected to be

* Corresponding author. Current address: School of Earth and Environmental Sciences, Seoul National University, 311 Ho, 25-1 Dong, San 56-1, Sillim-dong, Gwanak-gu, Seoul 151-747, Republic of Korea. Tel.: +82 2 880 6733; fax: +82 2 871 3269.
E-mail addresses: hjung@snu.ac.kr (H. Jung), ikuo.katayama@yale.edu (I. Katayama), zhenting.jiang@yale.edu (Z. Jiang), hirag001@umn.edu (T. Hiraga), shun-ichiro.karato@yale.edu (S. Karato).
[1] Tel.: +1 203 432 5990; fax: +1 203 432 3134.
[2] Tel.: +1 203 432 5791; fax: +1 203 432 3134.
[3] Tel.: +1 612 626 0572; fax: +1 612 625 3819.
[4] Tel.: +1 203 432 3147; fax: +1 203 432 3134.

0040-1951/$ - see front matter
doi:10.1016/j.tecto.2006.02.011

different from that in water-poor regions in which type-A fabric dominates (i.e., the lithosphere). A few cases are discussed including anisotropy in the subduction zone and in the deep upper mantle.

Keywords: Olivine; Lattice-preferred orientation; Water; Seismic anisotropy; Shear wave splitting; Plastic deformation

1. Introduction

The plastic deformation of olivine, the most abundant mineral in the Earth's upper mantle, plays an important role in controlling the dynamics and deformation microstructures in this region. The flow of mantle materials often results in anisotropic elastic properties mainly due to the development of lattice-preferred orientation (LPO) of olivine that can be determined from the naturally deformed peridotites (Ben Ismail and Mainprice, 1998; Mainprice et al., 2000) and can also be detected by seismological observations (Nicolas and Christensen, 1987). If a relationship between the LPO of olivine and the deformation geometry is known from the laboratory study, then one can infer deformation geometry and/or deformation conditions (such as water content) from observed deformation microstructures. Similarly using mineral physics data, one can calculate seismic anisotropy for the given deformation geometry and this can be used to interpret seismic anisotropy in nature. In most previous studies, the relationship between the LPO and deformation geometry obtained (or inferred) from samples deformed at relatively water-poor conditions have been used (Nicolas and Christensen, 1987; Mainprice et al., 2000). However, it is known that a large amount of water can be dissolved in olivine (Miller et al., 1987; Bell and Rossman, 1992; Kohlstedt et al., 1996; Wallace, 1998; Jung and Karato, 2001a,b) and water is known to have significant effect on the plastic deformation of olivine (Carter and Avé Lallemant, 1970; Chopra and Paterson, 1981, 1984; Mackwell et al., 1985; Karato et al., 1986; Mei and Kohlstedt, 2000a,b; Jung, 2002; Karato and Jung, 2003). And more importantly, water is known to change the relative strength of slip system of olivine even at the low pressure of 0.3 GPa with a small amount of water (Mackwell et al., 1985). Based on this observation, Karato (1995) proposed that olivine LPO might change with water content. The LPO of olivine can also be modified by grain boundary migration (Karato, 1987a). It is also known that water enhances grain boundary migration of olivine (Karato, 1989; Jung and Karato, 2001a). For these reasons, it is expected that water may have important influence on the LPO in olivine.

However, the details of how water affects the LPO of olivine have not been understood because previous experimental studies had following limitations. First of all, previous experimental studies were conducted in samples with relatively small water content (Nicolas et al., 1973; Zhang and Karato, 1995; Zhang et al., 2000; Bystricky et al., 2000; Lee et al., 2002). Secondly, the deformation geometry of the most previous studies was limited to triaxial compression with a small strain (Carter and Avé Lallemant, 1970; Avé Lallemant and Carter, 1970; Nicolas et al., 1973), although the deformation of the real Earth is most likely with a large strain with significant component of non-coaxial deformation geometry (Nicolas et al., 1971; Nicolas, 1976). The maximum strain achieved in triaxial compression experiments is ~ 0.6 due to the limitations of deformation geometry. Shear deformation experiments with large strain are essential to our understanding of the development of LPO of the real Earth. Thirdly, the triaxial compression deformation experiment is of limited relevance because both stress and strain orientations are same due to the coaxial deformation. In addition, high pressure is necessary to observe significant effects of water on the plastic deformation of olivine because a large amount of water can be dissolved in olivine only under high pressure (Kohlstedt et al., 1996). For example, water fugacity at the pressure of 2 GPa at 1473 K is ~ 13 GPa in contrast to the water fugacity of ~ 0.3 GPa at the pressure of 0.3 GPa. To extend our knowledge of the effect of water on the olivine LPO, we have conducted experiments in simple shear geometry at higher pressures (~ 2 GPa) than previous studies. A brief account of our study was reported in Jung and Karato (2001b) and Katayama et al. (2004). In this paper, we report the details of experimental results on the LPO of olivine and the change in deformation microstructures with water content and stress, and we discuss their implications for seismic anisotropy.

2. Experimental procedures

2.1. Starting materials and sample preparation

Starting materials are either hot-pressed synthetic olivine aggregates or single crystals of olivine from San Carlos, Arizona. The sample assembly is shown in Fig. 1. For single crystal as a starting material, a gem-

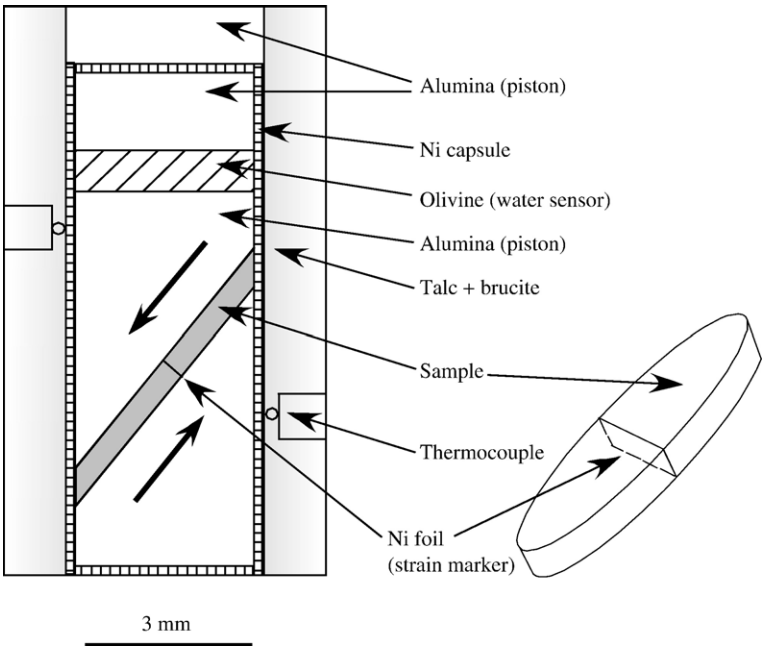

Fig. 1. A sample assembly with a simple shear design. Water is added to a sample by the decomposition of a mixture of talc and brucite during the experiment. A thin Ni foil is used as a strain marker.

quality olivine was oriented using a X-ray Laue diffraction pattern, core-drilled with a diameter of 3.2 mm, and sectioned to have various orientations as shown in Table 1. For the hot-pressed olivine aggregates, inclusion-free small single crystals of San Carlos olivine were hand-picked and crushed in an agate mortar. Powder was dried for 20 h at 1473 K in a CO/CO_2 gas-controlled furnace to give $f_{O_2}=10^{-5}$ Pa. Argon gas was flushed through the furnace to prevent carbon precipitation below 973 K. The dried specimens were kept in an oven at 423 K until they were used. For the water-poor samples, no water was added during the cold-press. Olivine grains of ~ 20 μm size were cold-pressed at the pressure of ~ 100 MPa. For the water-rich samples, we added ~ 20 μl of water during the cold press to enhance grain growth while sample was hot-pressed. After a cold press, samples were hot pressed at $P=300$ MPa and $T=1573$ K using a gas-medium Paterson apparatus. We dried the water-poor sample after hot-pressing in a CO/CO_2 gas-controlled furnace at $T=1473$ K for ~ 20 h. Samples were kept in an oven at $T=423$ K until used.

2.2. Deformation experiments

Deformation experiments were conducted using the Griggs apparatus in approximately simple shear geometry (Fig. 1) under both water-rich and water-poor conditions at the pressures of $P=0.5$–2.1 GPa and the temperatures of $T=1470$–1570 K. In water-poor experiments, water contents are typically less than ~ 200 ppm H/Si (for water content measurements see later part of this section). Pressure was raised first to a desired value in ~ 5 h and kept constant. The uncertainty in pressure estimation is due mainly to the friction (Mirwald et al., 1975) and the application of a deviatoric stress and is less than ~ 10%. Temperature was raised over ~ 1 h. Two thermocouples (Pt–Pt13% Rh) were placed close to the sample (Fig. 1): one close to the center of the sample, and the other close to the top of the sample. The temperature differences recorded by the two thermocouples imply uncertainties of 10–20 K. We used the temperature reading from the thermocouple close to the center as an estimated sample temperature. Temperature was reported without correction of the pressure effect on thermocouple emf. The pressure effect on thermocouple emf is less than ~ 10 K at 2 GPa (Getting and Kennedy, 1970). After the stabilization of temperature, a piston was advanced at a constant rate using a stepping motor for a constant strain-rate deformation. Deformation experiments were carried out to shear strains up to $\gamma \sim 6$. Experimental conditions are given in Table 1. Water was supplied to the sample by the mixture of talc and brucite surrounding a Ni capsule (Fig. 1). This mixture decomposes to water, olivine, and enstatite at ~ 1073 K and 2 GPa and the hydrogen penetrates to the sample through the Ni-capsule. The oxygen fugacity was buffered by the

Table 1
Experimental conditions and results

Run no.	P (GPa)	T [a] (K)	Fabric type	Water content [b] (ppm H/Si)	Compressional strain (%)	Shear strain [c] (γ)	Shear strain rate [d] (s^{-1})	Differential stress [e] (MPa)	M-index [f]
JK8 [g]	1.9	1470	B	1200	22	1.0 (±0.1)	$9.5\ (\pm1.3)\times10^{-4}$	340 [h]	0.03
JK11	2.1	1470	C	1300	25	1.1 (±0.1)	$9.2\ (\pm1.3)\times10^{-5}$	230	0.27
JK18 [i]	1.9	1470	C	1310	27	1.2 (±0.1)	$9.5\ (\pm1.3)\times10^{-4}$	300	0.08
JK21 [i]	2.0	1570	B	200	26	4.0 (±0.6)	$7.9\ (\pm1.5)\times10^{-5}$	410 [h]	0.21
JK23	2.0	1470	C	1000 [j]	33	4.0 (±0.5)	$1.8\ (\pm0.3)\times10^{-4}$	180	0.10
JK24	2.0	1470	C	1100	10	0.8 (±0.1)	$1.4\ (\pm0.2)\times10^{-5}$	160	0.26
JK25	2.0	1470	C	450 [k]	20	0.8 (±0.1)	$5.6\ (\pm0.8)\times10^{-6}$	290	0.20
JK26	1.0	1470	C	700	13	1.0 (±0.1)	$2.1\ (\pm0.3)\times10^{-4}$	250	0.23
JK40 [g]	1.9	1470	C	1200	26	0.9 (±0.1)	$3.9\ (\pm0.6)\times10^{-4}$	230	0.05
JK41 [g]	2.0	1460	C	1300	5	0.6 (±0.1)	$1.3\ (\pm0.3)\times10^{-4}$	160	0.06
JK43 [g]	0.5	1570	A	100	7	1.2 (±0.2)	$3.7\ (\pm0.7)\times10^{-5}$	260	0.06
JK47	0.5	1570	E	400	5	0.7 (±0.1)	$1.1\ (\pm0.1)\times10^{-4}$	110	0.40
GA12	2.0	1470	E	560 [l]	10	1.2 (±0.1)	$8.5\ (\pm0.4)\times10^{-5}$	230	0.28
GA23	2.0	1470	E	630 [l]	8	0.8 (±0.1)	$8.7\ (\pm0.3)\times10^{-5}$	190	0.26
GA25	2.0	1470	E	280 [l]	11	6.3 (±0.6)	$1.6\ (\pm0.2)\times10^{-4}$	320	0.44
GA38 [g]	0.5	1470	E	210 [l]	7	0.6 (±0.1)	$3.1\ (\pm0.2)\times10^{-5}$	190	0.07
GA 98	2.0	1470	B	640	12	2.5 (±0.3)	$1.9\ (\pm0.2)\times10^{-4}$	350 [h]	0.07

[a] We measured temperature from the thermocouple which was close to the center of the sample. The uncertainty is within ±10 K during the experiments.

[b] Water content of olivine crystals was measured by FTIR using a calibration of Paterson (1982). If a new calibration by Bell et al. (2003) is used, the results should be multiplied by a factor of ~ 3.5. The uncertainty of water content measurement (~ ±100 ppm H/Si) is mainly from the determination of the baseline of the IR spectrum. Water content is in atomic ppm H/Si.

[c] Shear strain was measured from the rotation of strain marker. The uncertainty of the strain comes from the heterogeneous shape of strain marker of each sample. When strain marker was not straight, we averaged the strain from the maximum and the minimum strain of the sample.

[d] The uncertainty of strain rate was calculated from the uncertainties of shear strain and hit points of the experiments.

[e] Differential stress ($\sigma_1-\sigma_3$) was measured from the dislocation density of the samples at the end of the run (except for the type-B samples). Uncertainty of the stress estimation was ~ ±10–15%.

[f] M-index is the misorientation index recently proposed which shows fabric strength of sample (see text for details).

[g] Starting materials are hot-pressed olivine aggregates.

[h] Results from the flow law by Karato and Jung (2003). Since the dislocation distribution was so heterogeneous, we estimated the stress using the flow law of olivine. The error bars of stress estimation from flow law are ~ ±20% (Karato and Jung, 2003).

[i] Starting material is single crystal olivine that was oriented in a sample assembly to activate (010)[100] slip system for JK18 and (001)[010] for JK21. Other samples (single crystal) as a starting material in the Table 1 were oriented to activate (001)[100] slip system (the third orientation).

[j] Water content of this sample was moderate (water content ~ 800 ppm H/Si) because of the melting of the mixture of talc + brucite.

[k] This is the minimum water content of the sample because of the water loss after long deformation experiment.

[l] Water content of this sample was small because of the melting of pressure medium.

Ni/NiO reaction (NiO was detected next to the Ni capsule after most of runs). A thin Ni foil (6 μm thick), inside the sample (Fig. 1) acted as a strain marker. Shear strain was calculated after each experiment by measuring a rotation angle of the strain marker (initially vertical to the shear plane). Compressional strain was also calculated by measuring the thickness of sample before and after each experiment. Compressional strain was ~ 5–30% depending on the shear strain of a sample (Table 1). The compressional strain was relatively small less than ~ 25% of the shear strain so that the LPO due to the compressional strain is considered to be small. In addition, a single crystal olivine (a water sensor, ~ 500 μm thick) with the orientation [010] axis parallel to the compression axis was inserted close to the sample to check the water content after each experiment (Fig. 1).

2.3. FTIR study

We used FTIR (Fourier transformation infrared spectroscopy) to determine the water content of the sample both before and after the experiments. Deformed olivine samples were polished on both sides down to 50–200 μm thick and were kept in an oven at T=423 K for more than 2 days prior to measurement by FTIR. In most cases, we measured water content in a single crystal (a water sensor). In this study, the quoted water contents exclude grain boundary water. We focused an infrared beam on a single crystal area using unpolarized transmitted light. A typical FTIR spectrum after deformation experiment in water-rich condition is shown in Fig. 2. The calibration by Paterson (1982) was used to calculate the amount of water from the infrared beam absorption in

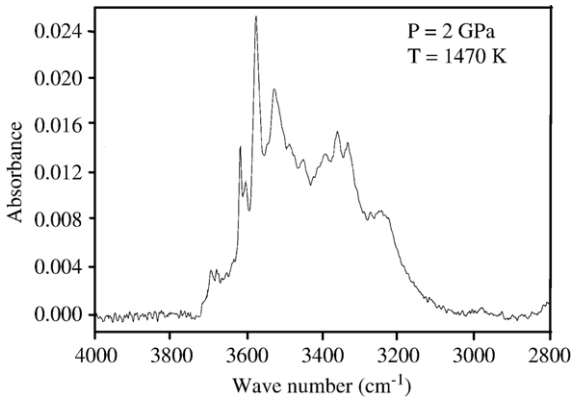

Fig. 2. A typical FTIR spectrum of the sample (JK23) after a deformation experiment in water-rich condition at the pressure of 2 GPa and the temperature of 1470 K. Spectrum was taken from the single crystal water sensor (130 μm thick) without including grain-boundaries with an unpolarized IR beam incident along the [010] direction.

the range of wave number 3000–3750 cm^{-1}, the region dominated by the stretching vibrations due to O–H bonds. The newer calibration by Bell et al. (2003) results in higher estimates by a factor of ~ 3.5. However, the physical basis for this new calibration is unclear, and we decided to report the results based on the Paterson calibration (if needed a correction can be made based on the new calibration). The water contents of the sample before experiments was ~ 20 ppm H/Si. The water contents of sample after experiments are shown in Table 1. The uncertainty of the FTIR measurement is within ~ ±100 ppm H/Si mostly due to the uncertainty in defining the baseline of infrared absorption spectrum.

2.4. Stress estimation

An accurate stress measurement of the sample is not simple for the solid-medium apparatus because of the friction involved in the external load cell (Gleason and Tullis, 1993). Although the use of a molten salt cell (or similar soft sample assembly, e.g., Green and Borch, 1989) reduces the problem of friction, it is not clear if the effects of friction can be removed entirely. Also, the use of talc and brucite as a pressure medium to add water makes it difficult to use a molten salt assembly. Therefore in this study, we used the dislocation density of deformed olivine to infer the stress magnitude using an SEM technique (Karato and Lee, 1999; Jung and Kararo, 2001a; Karato and Jung, 2003). The relationship between applied stress and dislocation density can be described empirically as follows (Kohlstedt et al., 1976a):

$$\rho = \alpha b^{-2}(\sigma/\mu)^m \quad (1)$$

where α is a non-dimensional constant, b is the length of the Burgers vector of dislocations, σ is stress, μ is the shear modulus, and m is a constant. This relation is nearly universal and is insensitive to the pressure at least in the pressure range of this study. We calibrated the relationship between free dislocation density (ρ) and applied stress (σ) of the olivine samples that were deformed at known stress levels using a gas-medium apparatus. Dislocations of olivine can be observed using a scanning electron microscope (SEM) (Karato, 1987b; Jung and Karato, 2001a). We determined non-dimensional parameters in Eq. (1) for polycrystalline olivine: $\alpha = -2.96 \pm 0.27$ and $m = 1.42 \pm 0.12$, and stress (σ) is in MPa and dislocation density (ρ) is in $10^{12}/m^2$(Jung, 2002; Karato and Jung, 2003). The uncertainties of the stress estimation are ~ ±10–15% from the calibrations and the heterogeneity of the dislocations in a single sample (i.e. Fig. 3). We measured dislocation densities from ~ 20 to 30 grains and averaged them to get a stress of a sample. The estimated stress of samples is summarized in Table 1. This technique works for the samples of type-A, type-C, and type-E where dislocation distribution is more or less homogeneous, but not well for some of the type-B samples where dislocation distribution is highly heterogeneous. For the type-B samples, we estimated the stress magnitude using the flow law of olivine (Karato and Jung, 2003) from the known temperature, pressure, strain rate, and water fugacity.

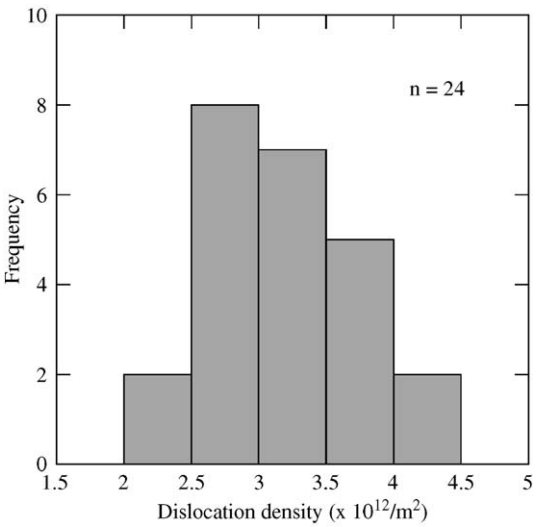

Fig. 3. A histogram showing the distribution of dislocation density (sample JK18). Dislocation density was measured from the back-scattered electron images (BEI) of the individual grains (n=24) after the sample was decorated by oxidation in the air. Mean dislocation density of the sample is $3.2 \times 10^{12}/m^2$.

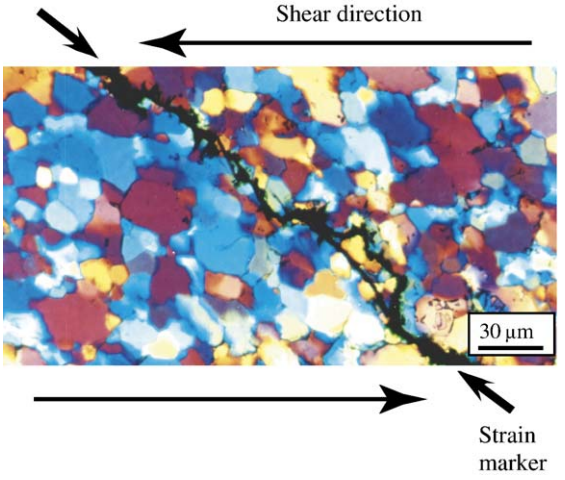

Fig. 4. A transmitted polarized-light micrograph of a deformed sample (JK18) showing the stain marker (Ni foil). The black line represents the strain marker with a rotation angle of ~ 51° (γ = 1.2) from the vertical (initial) orientation. The sense of shear is top to the left. This figure also shows an example of a total recrystallization from a single crystal in water-rich condition at the shear strain of $\gamma \sim 1$.

2.5. Measurement of olivine LPO

To determine the lattice-preferred orientation (LPO) of olivine, we used electron backscattered diffraction (EBSD) (Dingley, 1984, 1992; Lloyd, 1987; Prior et al., 1999). A JOEL 840 SEM at the University of Minnesota and a FEG ESEM XL30 at Yale University equipped with HKL's EBSD system were used in this study. The spatial resolution of this system is about 1 μm. Samples were polished using the diamond paste of 1 μm grain size. To remove all the surface damages, specimens were then polished using the SYTON (a colloidal silica) fluid for chemical–mechanical polishing (Lloyd, 1987). The specimens were coated with ~ 3 nm thick carbon to prevent charging in SEM. The specimen surface was inclined at 70° to the incident beam. EBSD patterns were collected on a phosphor screen imaged by a low light SIT camera. We used an accelerating voltage of 30 kV and working distance of 25 mm and beam current of 10 nA at University of Minnesota while 20 kV and 15 mm were used at Yale University. All EBSD patterns of olivine were manually indexed using HKL's Channel software.

2.6. TEM study

To understand dislocation microstructure of olivine in deformed samples, weak-beam dark-field (WBDF) images were taken under 300 kV using the transmission

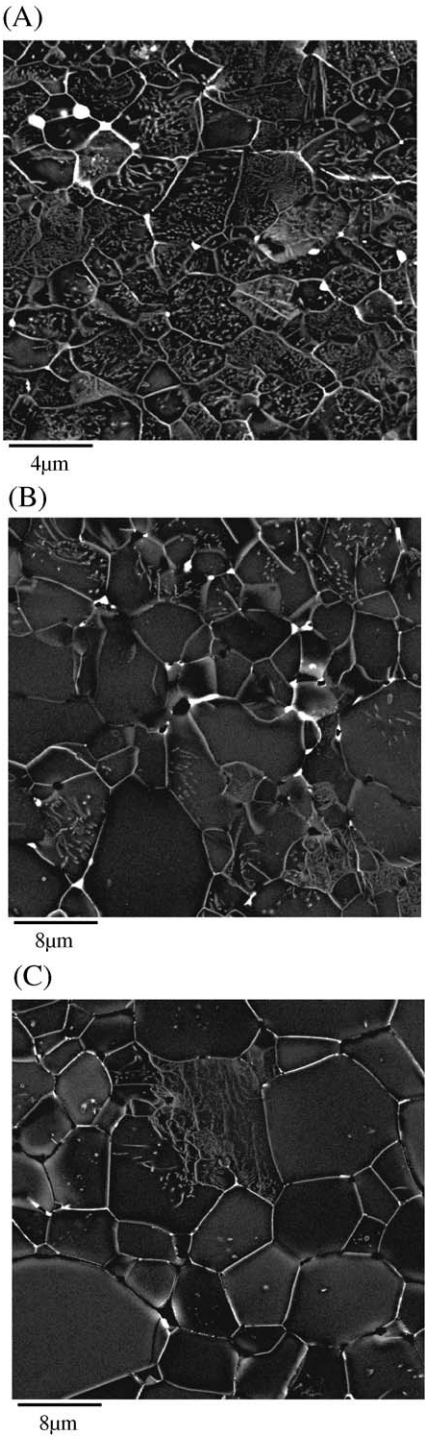

Fig. 5. Backscattered electron images showing dislocation microstructures of olivine samples deformed in type-B regime. Bright lines show grain-boundaries or dislocations. Note that dislocation distribution (density) changes markedly with water content (C_{OH}). (A) $C_{OH} \sim 200$ ppm H/Si (JK21), (B) $C_{OH} \sim 630$ ppm H/Si (JK45 from Jung and Karato, 2001b), (C) $C_{OH} \sim 1200$ ppm H/Si (JK8).

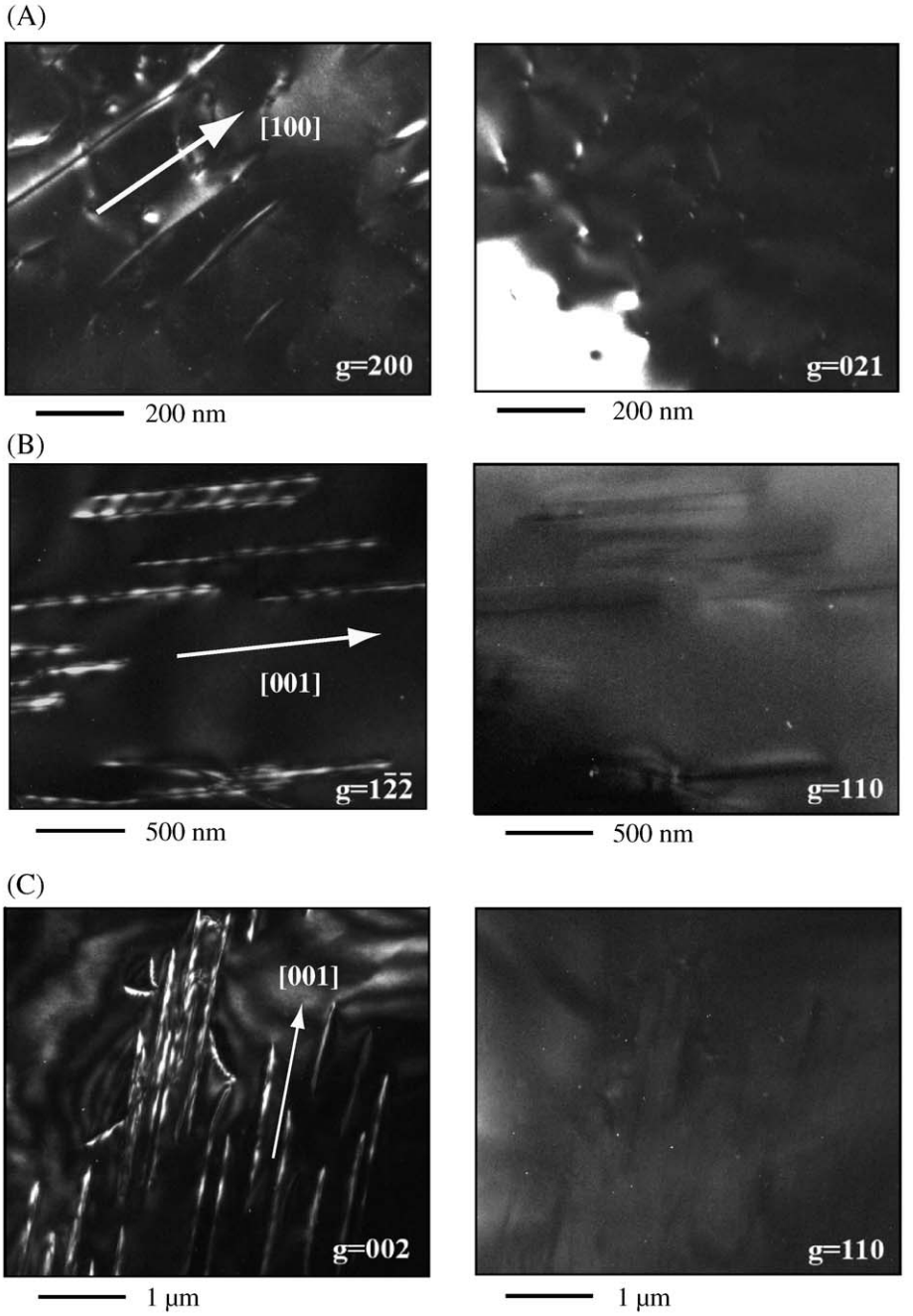

Fig. 6. Weak-beam dark-field (WBDF) TEM images of three different samples (type-A, B, and C). All images were taken under the reflections shown in every image. All dislocations have strong contrast in the left (column) images, while most of the dislocations at the same area lose their contrasts in the right image. (A) WBDF images of dry and low stress sample (MIT 21 from Zhang et al. (2000), type-A) under $g=200$ reflection (left) and $g=021$ (right), respectively. The dislocations are edge dislocations since they are parallel to *a*-axis. (B) WBDF images of water-rich and high stress sample (JK8, Type-B) under $g=1\bar{2}\ \bar{2}$ (left) and $g=110$ (right) reflections, respectively. (C) WBDF images of water-rich and low stress sample (JK11, Type-C) under $g=002$ and $g=110$ reflections, respectively. Most of the observed dislocations in both (B) and (C) are *c*-screw which are majority in wet samples.

electron microscope (TEM) of Philips CM30 at University of Minnesota. WBDF gives clear images of dislocation lines such as white narrow lines on a dark gray background. However, if the Burgers vector **b** satisfies invisible criteria, which are $\mathbf{g}\cdot\mathbf{b}=0$ for screw dislocation and $\mathbf{g}\cdot\mathbf{b}=0$ and $\mathbf{g}\cdot(\mathbf{b}\times\mathbf{u})=0$ for edge dislocation (**g** is the diffraction vector and **u** is a unit vector parallel to the dislocation line), the dislocation lines lose their contrast (McLaren, 1991). From these criteria, the direction of Burgers vector **b** was determined. Thin specimens for TEM observations were prepared from thin sections parallel to *XZ* plane of the samples (parallel to shear direction and perpendicular to shear plane), and finally ion-milled with an accelerating voltage of 3 kV and at an angle of 10–

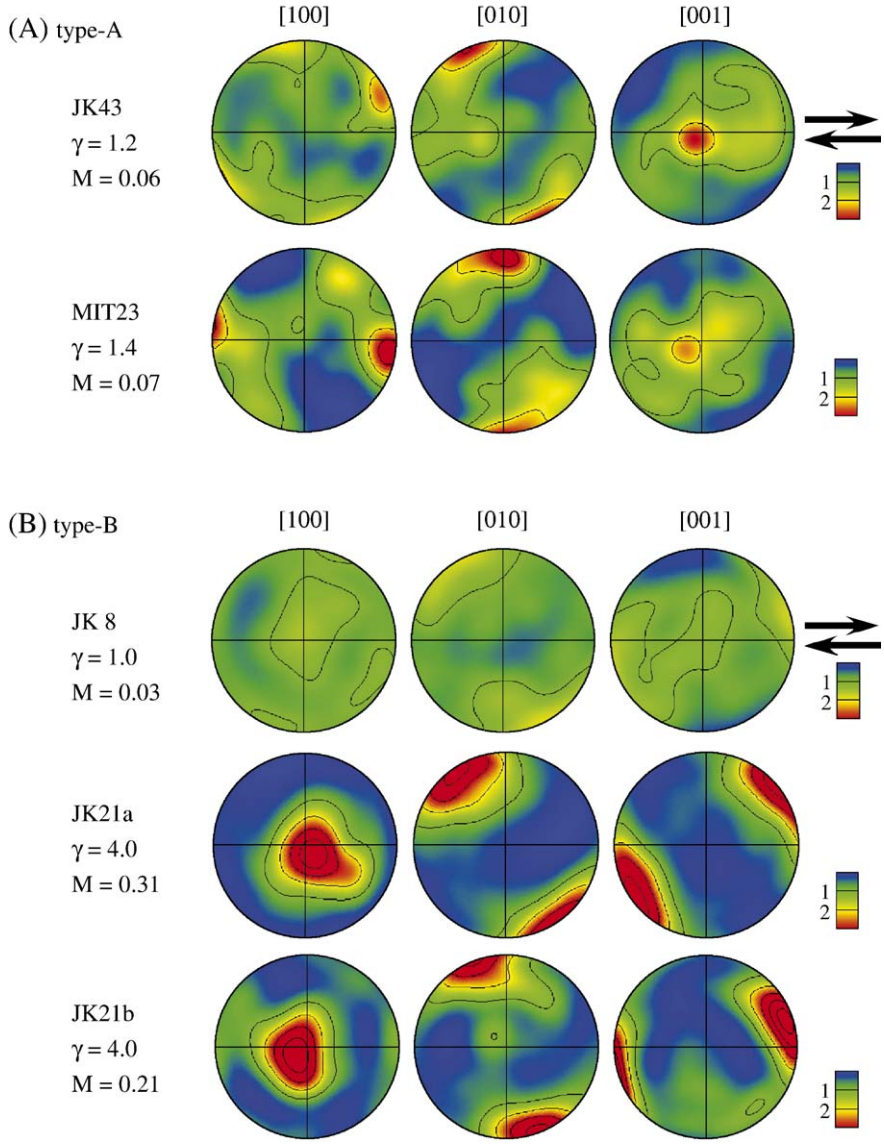

Fig. 7. Pole figures showing the lattice-preferred orientation (LPO) of olivine (type A, B, C, and E) with increasing shear strain. Pole figures are presented in the lower hemisphere using an equal area projection. The sense of shear is represented by the arrows. The north (south) poles correspond to the shear plane normal. We used a half scatter width of 30°. The color coding refers to the density of data points (contours in the pole figures correspond to the multiples of uniform distribution). Crystallographic orientations of ~ 200–500 grains of each sample were measured manually by the EBSD technique. γ and M represent the shear strain and the M-index (fabric strength), respectively. One of the dry samples in type-A (MIT23) is from Zhang et al. (2000). In the type-B pole figures, JK21a shows the LPO of partially recrystallized area and JK21b shows the LPO of totally recrystallized area of the specimen JK21.

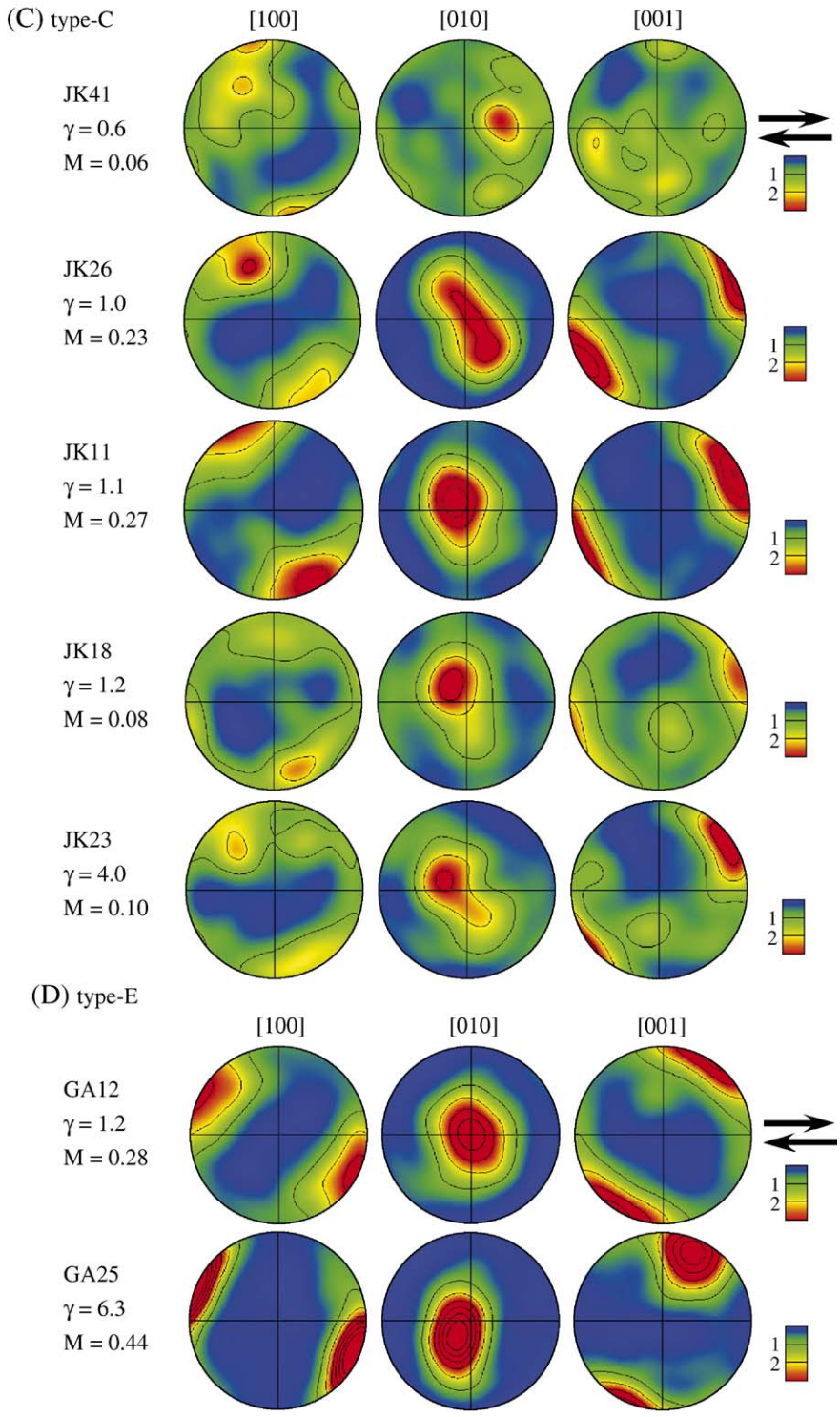

Fig. 7 (*continued*).

15°. The grains were easily separated during the milling for the water-rich samples that may be due to the presence of microcracks along the weak grain boundaries possibly because of water. Therefore, to prevent the plucking of grains during the milling, washers with grids were used or samples were embedded into epoxy first

and then milling only from one-side were performed for the water-rich samples such as JK8, 11 and 18. Finally, the specimens were carbon coated to prevent a charging in TEM.

2.7. Fabric strength

Fabric strength is often calculated using the so-called *J*-index (e.g., Bunge, 1982; Mainprice and Silver, 1993), but recently Wenk (2002) and Skemer et al. (2005) demonstrated that the J-index is sensitive to a number of parameters used in the calculation (e.g., a number of grains used in the measurements). Therefore, we used the misorientation index (*M*-index; Skemer et al., 2005) to calculate the fabric strength. A misorientation angle is defined as the minimum angle required to rotate two grains into concordance around a common axis. The *M*-index is defined as:

$$M \equiv \frac{1}{2}\int |R^T(\theta) - R^0(\theta)|\mathrm{d}(\theta) \quad (2)$$

where $R^T(\theta)$ is the theoretical distribution of misorientation angles for a random fabric, $R^0(\theta)$ is the observed distribution of uncorrelated misorientation angles. Individual misorientations were calculated from the EBSD data. The theoretical distribution for a random fabric depends on crystal symmetry. We used the distribution for orthorhombic crystals (Girimmer, 1979). The results of *M*-index are shown in Table 1.

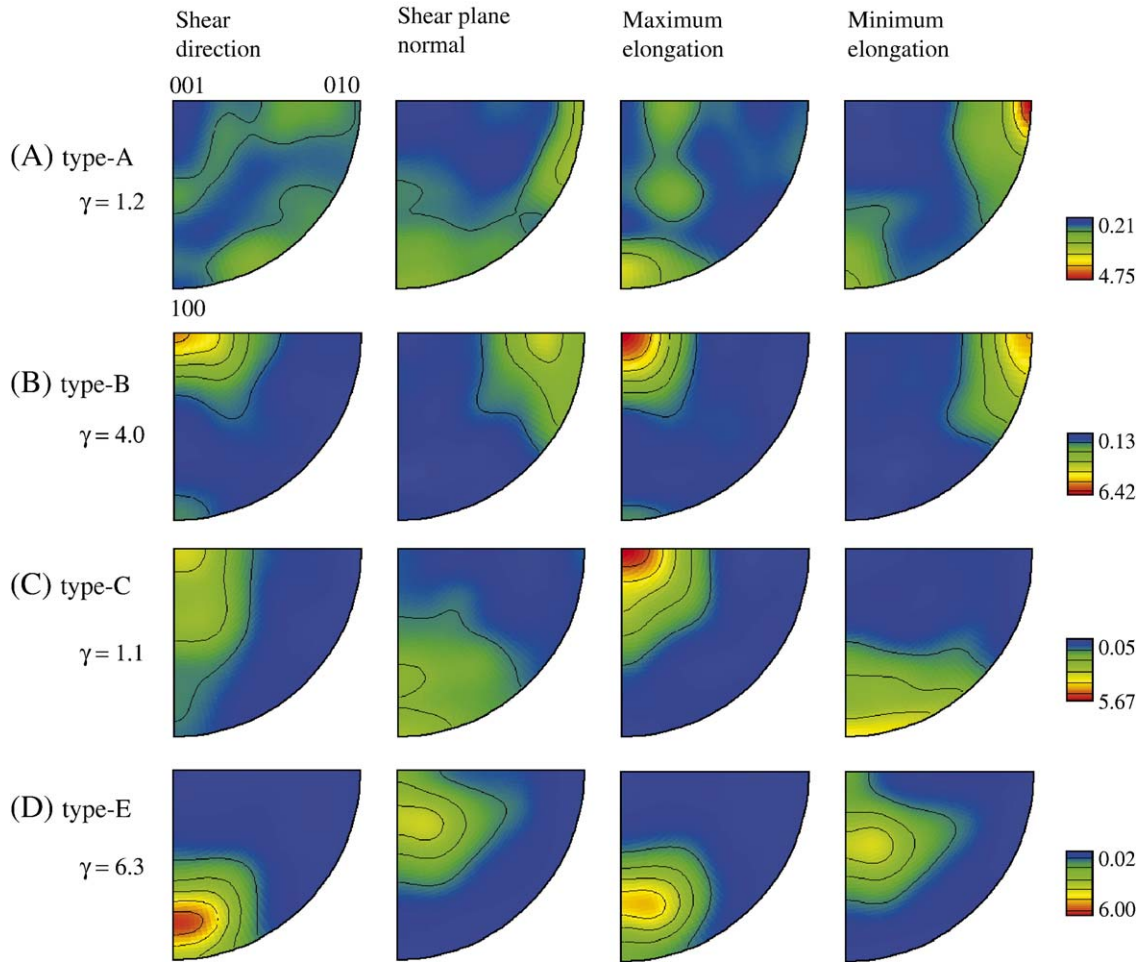

Fig. 8. Inverse pole figures of type-A, B, C, and E. (A) type-A (JK43), (B) type-B (JK21), (C) type-C (JK11), and (D) type-E (GA25). Inverse pole figures are shown in terms of the shear direction, the shear plane normal, the maximum elongation direction of strain ellipsoid, and the minimum elongation of strain ellipsoid that is 90° away from the maximum elongation direction of the strain ellipsoid. We used a half scatter width of 20°. The color coding refers to the density of data points (the numbers in the legend correspond to the multiples of uniform distribution).

3. Results

3.1. Water content

The experimental conditions and results are summarized in Table 1. FTIR data showed that solubility of water in olivine increased with increasing pressure at 0.5–2 GPa. Solubility of water in olivine at P=0.5, 1, and 2 GPa was ~ 400, ~ 700, and ~ 1200 ppm H/Si, respectively (Table 1). These results are consistent with the results by Kohlstedt et al. (1996), and therefore we conclude that most of our samples were under nearly water-saturated conditions.

3.2. Deformation geometry and deformation microstructures

Shear strain maker (Ni foil) after a typical simple shear experiment (JK18) under water-rich condition is shown in Fig. 4. The measurements of tilt of a strain marker and the thickness of samples indicate that the deformation geometry in these experiments was nearly simple shear with a small contribution from compression (~ 5–30%). Deformation is in most cases nearly homogeneous, but deformation in the both ends of a sample close to the capsule is always heterogeneous. Dislocation densities in these regions are lower than in the central regions indicating that microstructures in these regions reflect annealing. Consequently, all of our microstructural studies including LPO measurements and SEM and TEM studies of dislocation structures are on the central regions.

Optical microscope observations of deformed samples showed that grains are elongated slightly depending on the amount of strain (Fig. 4). Dynamic recrystallization is observed in all of the samples. Evidence of both subgrain rotation and grain-boundary migration is found. Grain-boundary migration modifies the grain-boundary morphology. However, the way in which grain-boundary migration modifies the grain-boundary morphology depends on the physical and chemical conditions.

In type-A sample (water-poor conditions), a large number of subgrain boundaries are observed in backscattered electron images after a sample was decorated with oxygen (Kohlstedt et al., 1976b; Karato, 1987b; Jung and Karato, 2001a), and grain-boundaries are curved (Jung and Karato, 2001b). In type-C samples (water-rich conditions), subgrain boundaries are rare and grain-boundaries are less wavy (Jung and Karato, 2001a,b). In type-E samples, dislocations show mostly linear structure with the [001] direction, and some dislocations are organized into tilt boundaries on the (100) plane, although subgrain-boundaries are rare. The dislocation microstructures of the type-B samples are remarkably different from that of type-A, type-C or type-E samples: dislocation densities of grains in type-B samples are generally highly heterogeneous (Fig. 5). In type-B samples, there is a trend that the number of the grains with low dislocation density increases with increasing water content (Fig. 5). The sample with water content ~ 630 ppm H/Si showed ~ 60% of grains dislocation-free (Fig. 5B). The sample with water content ~ 1200 ppm H/Si showed much more heterogeneous dislocation density distribution with ~ 90% grains dislocation-free (Fig. 5C). Grain boundary migration under water-rich condition is much faster than that under water-poor condition and may have affected dislocation microstructures. But, it is not clear yet for the formation of such a heterogeneous dislocation microstructures in the type-B samples.

Fig. 6 shows weak-beam dark-field TEM images of the three types of the samples (type-A, B, and C). The images in the left and right side were taken from the same area of a sample under different reflections. In the left images (left column), dislocations are observed as clear white lines, however, most of the dislocations in the right images (right column) lose their contrasts. This indicates that the observed dislocations satisfy the invisibility criterion for using the reflection of **g** in the right-side images. In addition, we took several images under different reflections to characterize the dislocations.

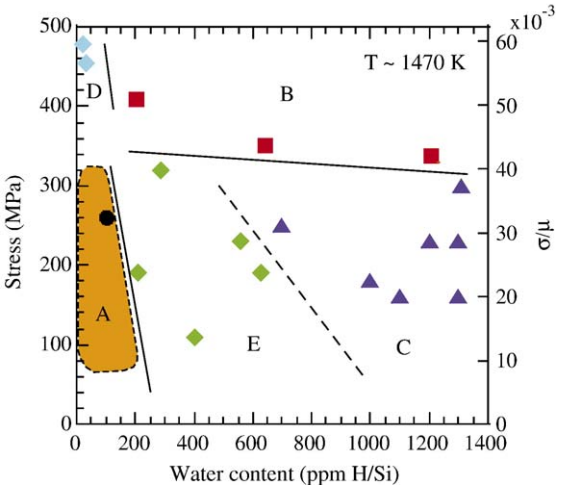

Fig. 9. A fabric diagram of olivine at T ~ 1470–1570 K (T/T_m ~ 0.7–0.75) showing the dominant fabric as a function of stress and water content (C_{OH}). Data for the type-A are from both this study (solid circle) and Zhang et al. (2000). Data for the type-B, C, and E are from Jung and Karato (2001b), Katayama et al. (2004), and this study. Data for the type-D are from Zhang et al. (2000) and Bystricky et al. (2000). Typical pole figures of each type of LPOs are shown in Fig. 10. Uncertainties of stress and water content measurements were given in Table 1 (refer to the captions of 2 and 5 in Table 1).

The TEM observations show that many dislocations in water-poor sample (type-A) are curved and tangled each other. Both **b**=[100] and **b**=[001] dislocations were observed in similar proportion. In type-B sample (JK8), few grains contain dislocations, however, grains with high dislocation density are occasionally found. The dislocations are mostly straight and distributed homogeneously in the grains. We found that most of them are **b**=[001] screw dislocations (Fig. 6B). Dislocations in type-B samples are not tangled and not interacting each other. We could not observe any sub-grain boundaries under TEM. In type-C samples (JK11 and JK18), dislocations are similar to those of type-B samples. They are straight and many are **b**=[001] screw dislocations (Fig. 6C). However, more **b**=[001] and **b**=[100] edge dislocations, and other dislocations with curved features are observed in type-C samples compared to those in Type-B samples. Furthermore, many straight dislocations are observed in type-C samples.

3.3. Lattice-preferred orientation

3.3.1. Olivine fabrics and a fabric diagram

Three new types (type-B, C, and E) of olivine LPO as well as a well-known type-A LPO have been identified in this study depending on the water content and stress. Pole figures of olivine [100], [010], and [001] axes after simple shear experiments are shown in Fig. 7. The sample which was deformed under low stress and water-poor conditions showed the LPO of olivine where [100] axis of olivine is subparallel to the shear direction, (010) plane subparallel to the shear plane (type-A, Fig. 7A). Samples deformed at relatively high stress under various water contents show an LPO in which olivine [001] axis subparallel to the shear direction, (010) plane subparallel to the shear plane. We call this LPO as type-B LPO. Samples deformed at high water contents at low stress conditions show an LPO in which olivine [001] axis subparallel to the shear direction, (100) plane subparallel

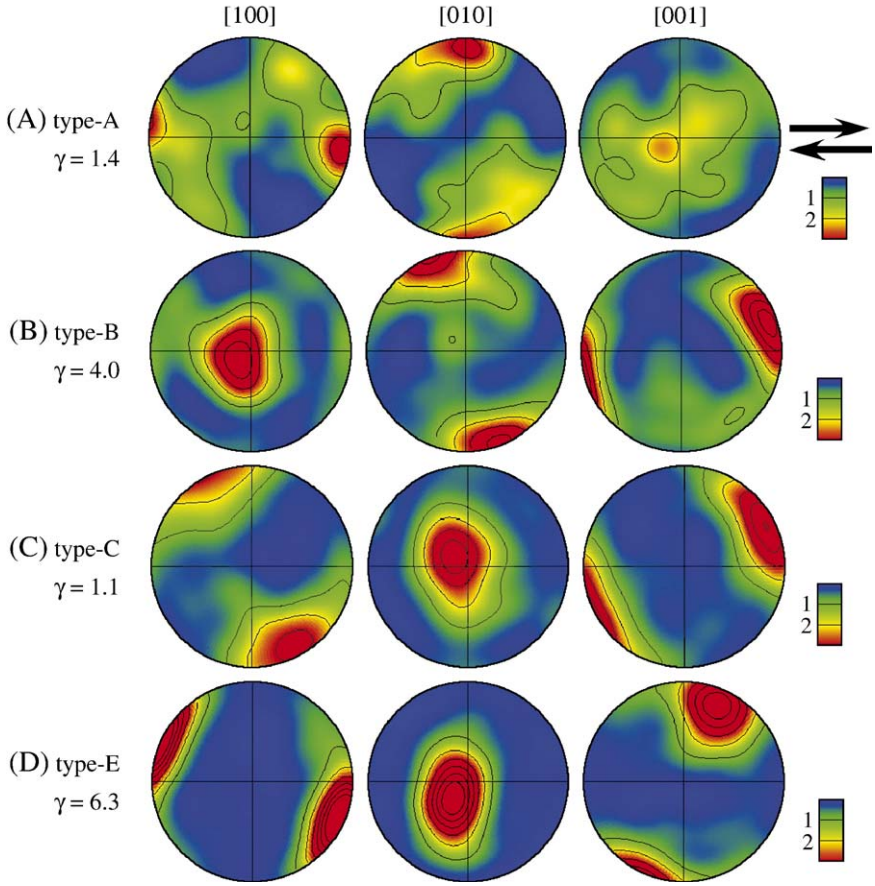

Fig. 10. Typical pole figures of type A, B, C, and E. (A) type A (MIT23), (B) type B (JK21), (C) type C (JK11), and (D) type E (GA25). Pole figures are presented in the lower hemisphere using an equal area projection. The sense of shear is represented by the arrows. The north (south) poles correspond to the shear plane normal. We used a half scatter width of 30°. The color coding refers to the density of data points (contours in the pole figures correspond to the multiples of uniform distribution). Other legends are the same as in Fig. 7.

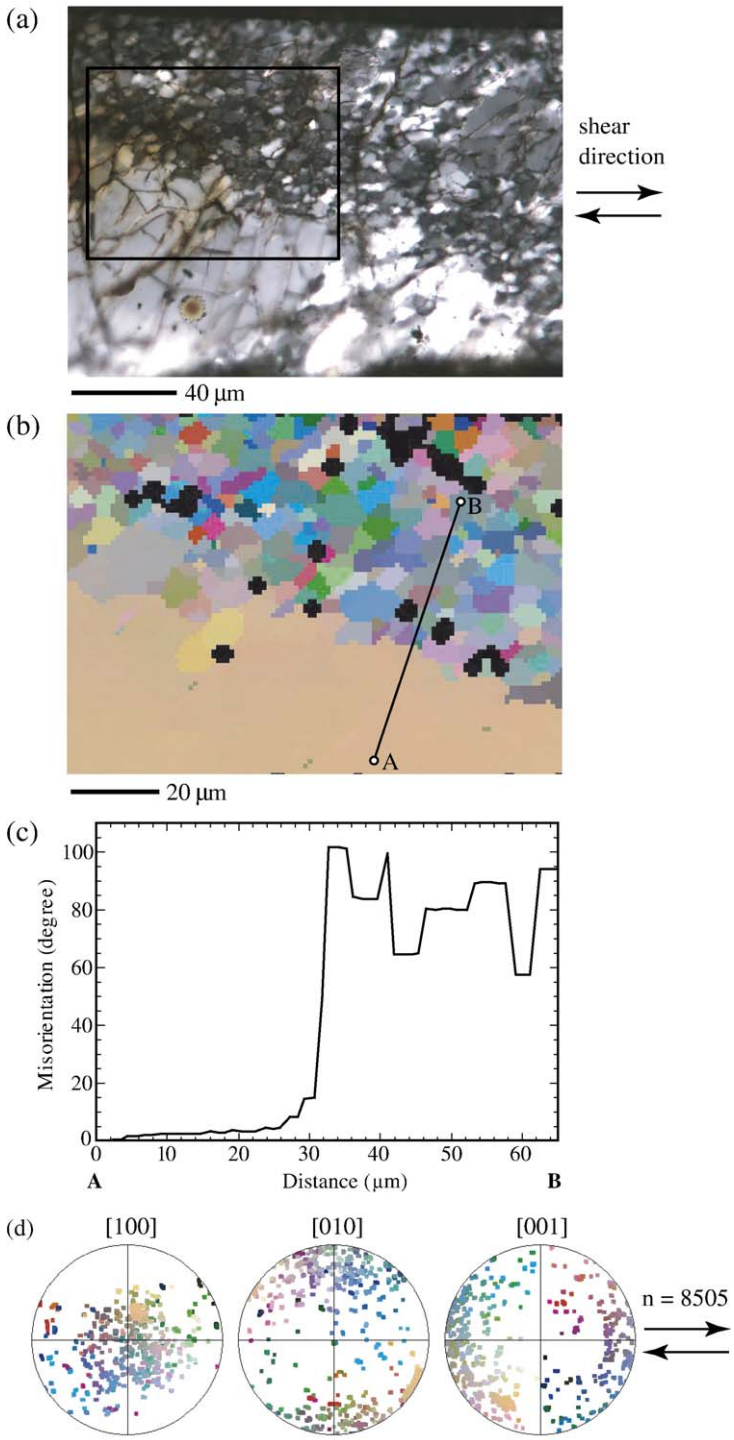

Fig. 11. (a) An optical microphotograph of JK21 showing the microstructure of a partially recrystallizaed olivine with a single crystal starting material. (b) EBSD mapping of a selected region shown in (a). (c) The misorientation angles of olivine relative to the orientation of olivine at point A along the A–B line. The misorientation angle abruptly changes at the boundary from the initial grain to the recrystallized grains. (d) Pole figure from the EBSD mapping (total 8505 points) showing the orientation of each grains (the color as same as that of (b)). Pole figures are presented in a lower-hemisphere and an equal area projection. Sense of shear is represented by the arrows (top to the right). The north (south) poles correspond to the shear plane normal.

to the shear plane. This LPO is called type-C LPO. At intermediate water content and low stress conditions, we found an olivine LPO that is characterized by olivine [100] axis subparallel to the shear direction, (001) plane subparallel to the shear plane (see also Fig. 8 for inverse pole figures in terms of shear direction and strain ellipsoid). This LPO is called type-E LPO. At water-poor conditions and high stress, olivine [100] axis subparallel to the shear direction, but its shear plane is not well defined showing that olivine [010] and [001] axes are in a girdle. We call this as type-D LPO (refer to Fig. 9). Typical pole figures for the type-A, B, C, and E samples are shown in Fig. 10.

The observed fabrics that depend on the stress and water content are summarized in a fabric diagram (Fig. 9). Boundaries between type-B and type-E (and type-C) are nearly a constant stress-line. In other words, the boundary between these types is stress sensitive but less sensitive to water content. In contrast, boundaries between type-A and type-E, and type-E and type-C are sensitive to water content but less sensitive to stress. Note also that this diagram is constructed from the data of a narrow temperature range (1200–1300 °C). The influence of temperature can be large and was investigated by Katayama and Karato (submitted for publication).

The role of dynamic recrystallization on olivine LPO was investigated in some detail using a sample that has been partially recrystallized (JK21). Fig. 11a shows an optical micrograph of a portion of the sample JK21 that includes both remaining single crystal and dynamically recrystallized grains. The orientations of grains in this region was determined by automatic EBSD mapping (Fig. 11b). The single crystal region has roughly the same orientation that is deviated somewhat from the starting orientation (due to strain-induced lattice rotation). This region, however, contains a large number of subgrains whose misorientation angles are less than ~ 3° (Fig. 11c). Within the "recrystallized" region, the misorientation angle increases abruptly (Fig. 11c), suggesting that the orientation of initial single crystal has little influence on the LPO of dynamically recrystallized regions.

Although some of our experiments were for polycrystalline starting materials, we also used single crystals as starting materials in some experiments. However, we found only small influence of initial orientation on the resultant deformation fabrics. This is due to the fast rotation of crystallographic orientation as documented by orientation mapping (see Fig. 11).

3.3.2. Inverse pole figures

Inverse pole figures of the type-A, B, C, and E samples are plotted in Fig. 8. The inverse pole figures are generated by plotting the direction of interest into the sample space. We present four types of inverse pole figures: shear direction, shear plane normal, maximum elongation direction of strain ellipsoid, and minimum elongation direction of strain ellipsoid that is 90° away from the maximum elongation of the strain ellipsoid. The orientation of finite strain ellipsoid was calculated from the rotation of the strain marker, assuming predominantly simple shear deformation. In the type-A sample, the [010] axis is subparallel to the shear plane normal and close to the minimum elongation direction, and there is a trend that [100] axis is subparallel to the maximum elongation direction. In the type-B sample, however, the olivine [001] axis is subparallel to the shear direction and close to the maximum elongation, while the [010] axis is close to the minimum elongation direction, indicating that the [001] axis is the glide direction and the (010) plane is oriented closed to the shear plane. In the type-C sample, the olivine [001] axis is subparallel to the

Table 2
Elastic constants C_{ij} (GPa) of olivine aggregates at 5 GPa, 1573 K

i	$j=1$	$j=2$	$j=3$	$j=4$	$j=5$	$j=6$
A-type fabric						
1	236.3	84.5	81.5	0.4	3.4	0.3
2		218.5	82.9	−1.8	1.2	0.3
3			208.0	−1.3	6.1	0.2
4				64.9	−0.1	−1.9
5					68.7	0.3
6						66.6
B-type fabric						
1	221.3	84.3	83.3	−0.3	0.8	1.6
2		223.5	81.7	−1.4	1.0	1.6
3			215.5	−1.3	1.1	−0.4
4				68.9	0.7	−0.4
5					67.4	−0.4
6						69.4
C-type fabric						
1	223.2	83.6	83.3	0.3	−3.7	0.3
2		209.8	81.9	0.8	1.5	0.3
3			228.5	0.4	−5.9	0.2
4				67.9	0.2	−1.9
5					71.1	0.3
6						66.6
E-type fabric						
1	236.8	82.3	84.1	−0.6	0.4	0.1
2		207.7	82.7	−2.6	−0.3	−1.0
3			217.4	−2.1	−1.9	−0.7
4				65.0	0.1	0.4
5					71.1	−1.4
6						68.5

Reference axes defined as 1: shear direction, 3: shear plane normal, and 2: perpendicular to both 1 and 3 directions.

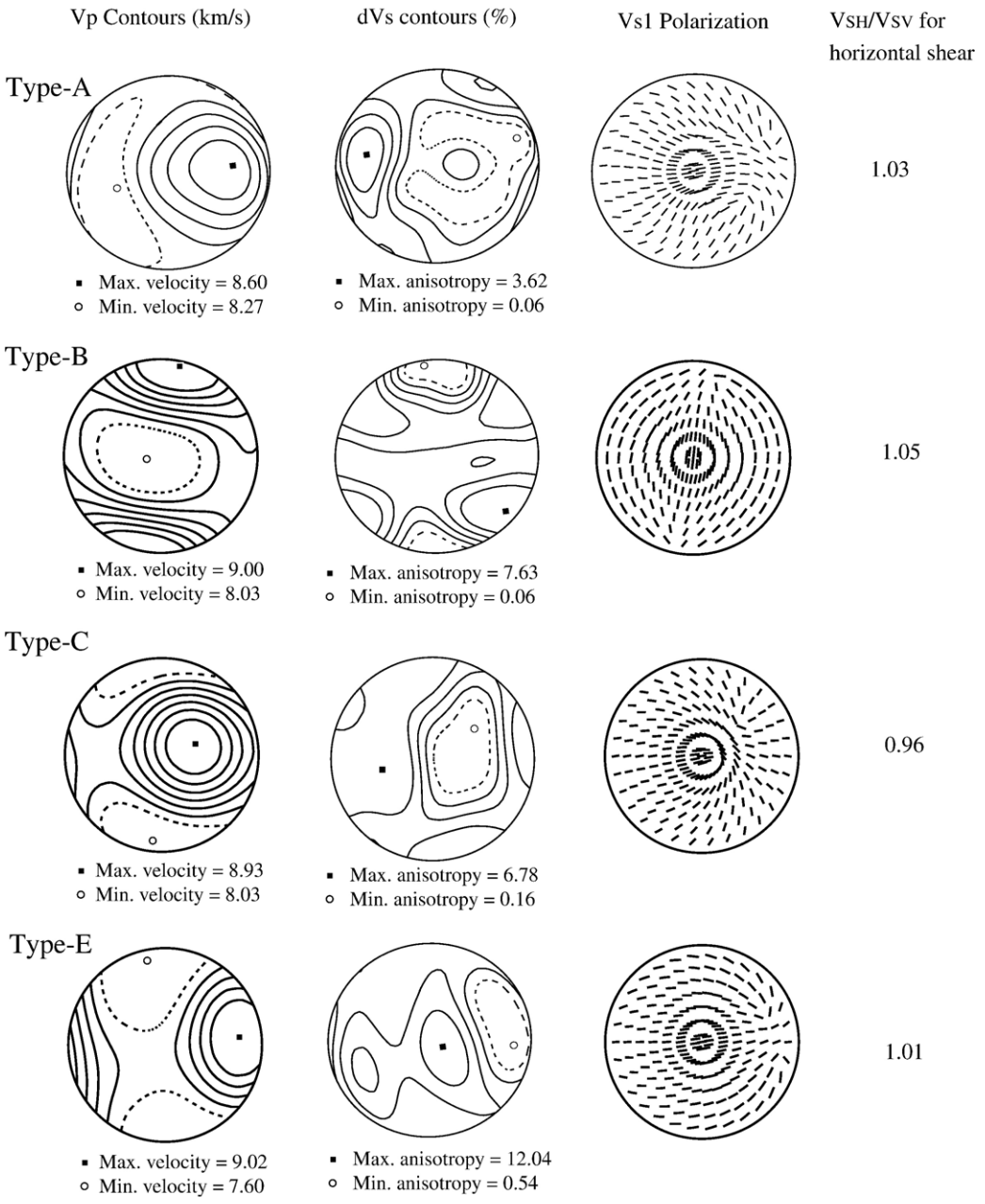

Fig. 12. Seismic anisotropy calculated from the elastic constants shown in Table 2. Anisotropy is shown on a stereographic projection in which the center of a plot is the direction normal to the shear plane, and the E–W direction corresponds to the shear direction. P-wave anisotropy, the amplitude of shear wave splitting (dVs) and the direction of polarization of the faster shear wave (Vs1) are shown.

shear direction, and the minimum elongation is close to the [100] axis. In the type-E sample, the olivine [100] axis is subparallel to the shear direction, and [001] axis is close to the shear plane normal. It is also observed that the deviation of the peak orientations from the shear direction appears to be large for the type-C sample.

In all cases except for the type-A fabric, the correlation between the inverse pole figures and the direction of strain ellipsoid (maximum elongation) is stronger than that between the inverse pole figures and the shear direction or shear plane normal (Fig. 8).

3.4. Seismic anisotropy

Given the distribution of crystallographic axes in a deformed polycrystal sample, one can easily calculate

Table 3
Seismic anisotropy due to different lattice preferred orientations of olivine

	A-type	B-type	C-type	E-type
Horizontal shear	$V_{SH}>V_{SV}$	$V_{SH}>V_{SV}$	$V_{SH}<V_{SV}$	$V_{SH}>V_{SV}$
Vertical shear	$V_{SH}<V_{SV}$	$V_{SH}>V_{SV}$	$V_{SH}>V_{SV}$	$V_{SH}<V_{SV}$
Polarization of fast S-wave	Parallel to flow	Normal to flow	Parallel to flow	Parallel to flow

$V_{SH\ (SV)}$ correspond to the velocity of horizontally (vertically) polarized S-wave.

the anisotropic elastic constants of the polycrystal and one can evaluate the nature of seismic anisotropy corresponding to a given LPO for a given flow geometry (Mainprice, 1990). From geological point of view, olivine fabrics with the type-A, B, C and E are most important in the upper mantle, and therefore we focus on these fabrics here. Table 2 lists the elastic constant matrix corresponding to these fabrics corresponding to simple shear flow on the $x_3=0$ plane along the x_1 direction. The elastic constants of olivine at 5 GPa and 1573 K (Abramson et al., 1997) were used in this calculation.

From the elastic constant matrix, one can calculate seismic wave velocities and resultant anisotropy. Fig. 12 and Table 3 summarize the results. Different olivine fabrics result in different types of seismic anisotropy. A few points are worth noting:

(i) If the flow plane is a horizontal plane, then olivine type-A, type-C and type-E LPO will show that the direction of polarization of the fast shear wave is subparallel to the flow direction, whereas for olivine type-B LPO, it is normal to the flow direction (Fig. 12).
(ii) If the flow is horizontal shear, then olivine type-A, type-B and type-E fabric will result in $V_{SH}/V_{SV}>1$ (in a transverse isotropy), whereas olivine type-C fabrics will result in $V_{SH}/V_{SV}<1$. The amplitude of this type of polarization anisotropy is mostly weak for the olivine type-C fabric.

Shear wave splitting and the V_{SH}/V_{SV} polarization anisotropy are most frequently observed types of seismic anisotropy. Consequently, the present results have important implications for interpreting seismic anisotropy in the Earth's upper mantle.

4. Discussions

4.1. Mechanisms of fabric transitions

For a given deformation geometry, the nature of lattice-preferred orientation is primarily controlled by the relative contribution of each slip system to the total strain (e.g., van Houte and Wagner, 1985). A change in the contribution from other processes such as grain-boundary migration may also influence LPO (e.g., Karato, 1987a). A large number of slip systems have been identified in olivine including (010)[100], (001)[100], {0kl}[100], {kl0}[001] (Carter and Avé Lallemant, 1970; Nicolas and Christensen, 1987). The relative contribution of different slip systems depends on the relative easiness of each slip system. In general, easy slip systems make a large contribution to the total strain and control the LPO development. The relative easiness of slip systems in turn depends on the physical and chemical conditions of deformation which will cause a fabric transition.

In this study, we have shown that the water content and stress magnitude have important effects on olivine LPO. Here we discuss the microscopic mechanisms by which the observed changes in LPO may have occurred. Our TEM observations clearly indicate that the deformation by **b**=[001] slip systems becomes easier with the addition of water (see also Sharp et al., 2003). This is consistent with the low-pressure results by Mackwell et al. (1985) (see also Karato, 1995). There are also changes in dominant glide planes. For example, previous study (Mackwell et al., 1985) suggests that the (001)[100] slip system becomes easier than the (010)[100] slip system by the addition of a small amount of water. With a larger

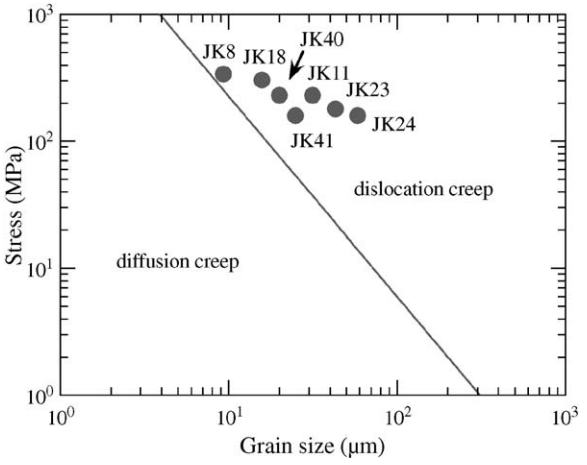

Fig. 13. A deformation mechanism map of olivine at $P=2$ GPa and $T=1473$ K under water-saturated condition using the recent experimental data (Mei and Kohlstedt, 2000a,b; Karato and Jung, 2003). The black line shows the boundary between dislocation creep and diffusion creep regime. This figure shows that recrystallized grain size under water-rich condition (water content ≥ 1000 ppm H/Si) is large and the sample was deformed in dislocation creep regime. Uncertainty of stress estimation was ~ ±10–15%. Grain size was measured by the linear intercept method using a scaling factor of 1.5 (Gifkins, 1970).

amount of water the (100)[001] slip system (and other **b**=[001] slip systems) are expected to become easier than the (010)[100] slip system (Karato, 1995). This is precisely what we found: the addition of water first changes the fabric from type-A ((010)[100] slip system) to type-E ((001)[100] slip system), and then at higher water content, type-C fabric ((100) [001] slip system) becomes important (Fig. 9). Therefore, a part of our observations can be attributed to the change in the dominant slip systems by the addition of water (and the change in the stress magnitude).

Various microscopic mechanisms may be responsible for the change in the strength of various slip systems. First is the selective reduction of the Peierls stress due to the addition of water. Katayama and Karato (in preparation) showed that the Peierls stress in olivine is reduced by water. Similar observation was made for quartz (Heggie and Jones, 1986). Second, alternatively, the number of jogs may change with water content differently for the different slip systems. In both cases, since the Burgers vector is longer for the **b**=[001] slip systems than the **b**=[100] slip systems, the influence of water is expected to be larger for the **b**=[001] slip systems than the **b**=[100] slip systems.

Given the relative importance of various slip systems, actual LPO is controlled also by the nature of strain accommodation. This is an important issue in olivine where there are only three independent slip systems. In such a case, even in cases where majority of strain is accommodated by dislocation creep, strain accommodation due to diffusion creep plays an important role. Note that the relative contribution from dislocation and diffusion creep in olivine under most of experimental conditions (and also in natural conditions) is rather similar (Karato et al., 1986).

The geometry of LPO determined by this study has rather large scatter due presumably to the less than ideal deformation geometry. However, we do have some robust observations on the geometry of LPO. As can be seen from Fig. 7, the orientation of dominant slip direction under water-rich conditions (i.e., **b**=[001]) never become parallel to the shear direction even at large strains. This is in marked contrast to the evolution of LPO under water-poor conditions (type-A fabric). This can be understood in terms of deformation mechanism map. Under water-poor conditions, the size of recrystallized grains is much smaller than the critical size for the transition between diffusional and dislocation creep, and consequently, the recrystallized regions deform more- or less by diffusional creep (Lee et al., 2002). This relaxes the constraint on deformation leading to a "single slip LPO". However, under water-rich conditions, the size of dynamically recrystallized grains become larger (Jung and Karato, 2001a) and recrystallized regions may deform largely by dislocation creep (Fig. 13). Under these circumstances, constraints on deformation would not be relaxed and hence LPO would follow the finite strain ellipsoid.

4.2. Scaling of a fabric diagram

Because some of the conditions in our experiments (particularly the strain-rates) are different from those in the Earth, we need to understand the scaling law for fabric transitions if our results were to be applied to the Earth. Without going to any details, we can make a simple analysis. Recall that any fabric transition occurs when the rates of two processes (e.g., strain-rates of two slip systems) become similar. Therefore a generic equation to define a fabric boundary is

$$A_1(T,P,C_{\mathrm{OH}},\sigma) = A_2(T,P,C_{\mathrm{OH}},\sigma) \tag{3}$$

where A_1 and A_2 are the rates of processes responsible for a fabric development (e.g. strain-rate), T is the temperature, P is the pressure, C_{OH} is the water content, and σ is the stress. Therefore, the transition conditions between two types of fabric are given by a hyper-surface defined as,

$$f(T,P,C_{\mathrm{OH}},\sigma) = 0. \tag{4}$$

In most cases, the rates of these processes can be given by a set of non-dimensional variables as

$$A'_1\left(\frac{T}{T_{\mathrm{m}}(P)}, C_{\mathrm{OH}}, \frac{\sigma}{\mu(P,T)}\right) = A'_2\left(\frac{T}{T_{\mathrm{m}}(P)}, C_{\mathrm{OH}}, \frac{\sigma}{\mu(P,T)}\right) \tag{5}$$

and consequently

$$f'\left(\frac{T}{T_{\mathrm{m}}(P)}, C_{\mathrm{OH}}, \frac{\sigma}{\mu(P,T)}\right) = 0. \tag{6}$$

Therefore, the boundaries between different types of LPO can be given by a hyper-surface in a multi-dimensional space that does not include strain-rate explicitly. The immediate consequence of this is that the fabric boundaries do not explicitly depend on strain-rates so that the fabric boundaries determined by laboratory experiments can be applied to the Earth's interior where deformation occurs at much slower strain-rates. The only difference between the laboratory and the Earth is that

because the laboratory experiments are conducted at much faster strain-rates than those in the Earth, laboratory studies can explore only a limited range of parameter space (e.g., relatively high stress regions). It also follows from Eq. (6) that in most cases, the fabric can be represented in a three-dimensional space, and our results shown in Fig. 9 must be considered to be a part of a more complete fabric diagram for a limited range of temperature. This scaling also allows us to compare our results with the results at different temperature and pressure conditions as we will show in the later section.

4.3. Some notes on related studies

We should also comment on two recent papers in which similar fabric transitions were reported but different causes were suggested. First, Holtzman et al. (2003) reported that olivine *c*-axis is subparallel to the maximum elongation and olivine *b*-axis is normal to the shear plane (B-type fabric) when olivine is deformed with a small amount of melt that contains a large amount of chromite or FeS. They noted that olivine fabric in their sample has strong *b*-axes normal to the shear plane, but both olivine *a*- and *c*-axes form a girdle when strong shear bands are not formed (their results are different from those by Zimmerman et al. (1999) who observed a typical A-type fabric in which olivine *a*-axis direction has a peak subparallel to the shear direction). After shear bands are clearly formed (at larger strains), olivine *a*-axes peak starts to strengthen normal to the shear direction. Holtzman et al. (2003) interpreted this evolution of olivine fabric in terms of deformation geometry. In their deformation set-up, a significant compression component exists and therefore extrusion of sample occurs. The "B-type fabric" that they observed is likely related to unusual deformation geometry caused by the geometry of sample assembly. Because of the constraints by the top and bottom pistons, the flow of material due to uniaxial compression will be normal to the shear direction. Otherwise there is no obvious reason for the selective extrusion normal to the shear direction. However, if this is the cause for this unusual observation of the olivine fabric, then the relevance of their observation to seismic anisotropy in the Earth is highly questionable. In fact, if such an olivine fabric develops beneath a mid-ocean ridge, one would expect anisotropic structure in the oceanic lithosphere that is totally inconsistent with observations. Therefore we conclude that the results of Holtzman et al. (2003) are of interest in a small-scale shear zone where deformation could deviate from ideal simple shear, but are unlikely to be relevant to the understanding of mantle flow in a global scale.

It must be emphasized that we assumed that the main role of confining pressure is to modify the relative easiness of dislocation slip systems through the change in water fugacity. This is reasonable because the water fugacity changes dramatically in this pressure range: from ~ 0.3 to ~ 13 GPa when pressure changes from 0.3 to 2 GPa (at ~ 1500 K). However, it is also possible that pressure has its intrinsic effects in changing the relative strength of different slip systems while keeping the water fugacity constant. Indeed, Couvy et al. (2004) recently suggested that the pressure may have an intrinsic effect to enhance the activity of the **b**=[001] slip systems relative to the **b**=[100] slip systems. Although this is an interesting possibility, we consider that this notion is speculative at this stage for the following reasons. Firstly, all samples that showed type-C fabric in Couvy et al. (2004) contain a high concentration of water. When their experimental conditions are compared with ours after normalization using the non-dimensional variables, T/T_m (P) and $\sigma/\mu(P,T)$, their experimental conditions are exactly in the domain in which one expects type-C fabric (stress is ~ 100–500 MPa ($\sigma/\mu = 1.2–6\times10^{-3}$), temperature is 1673 K and pressure is 11 GPa ($T/T_m \sim 0.70$), and water content is ~ 1500–2500 ppm H/Si). It is still possible that pressure may have an intrinsic effect to modify the mobility of different types of dislocation in a different degree to cause a pressure-induced fabric transitions, but in order to test this hypothesis, one needs to conduct a systematic experimental study in which LPO of olivine is determined as a function of pressure keeping other parameters nearly identical. Such a study has not been performed to our knowledge.

4.4. Some applications to deformation in the Earth

Numerous studies have shown that olivine LPO in naturally deformed peridotites is dominated by the type-A fabric (Mercier, 1985; Ben Ismail and Mainprice, 1998; Mainprice et al., 2000). However, majority of these previous studies have focused on geochemically depleted peridotites from the lithosphere which contain small water contents (e.g., Bell and Rossman, 1992), and our sampling is likely biased. The experimental studies in our laboratory suggest that other types of fabrics might be found in less depleted regions of the Earth's upper mantle, such as the upper mantle in convergent boundaries. In fact, new types of fabrics such as type-B, C, and E have been reported in rocks from convergent boundaries. The examples are the peridotites from Alpe Arami, Switzerland (Möckel, 1969; Buiskool Toxopeus, 1976, 1977; Frese et al., 2001, 2003), the peridotites from the Cima di Gagnone, Central Alps, Switzerland (Frese et al., 2001,

2003; Skemer et al., submitted for publication), the garnet peridotite from the Higashi-akaishi-yama, Shikoku, Japan (Yoshino, 1961; Mizukami et al., 2004), the mylonite peridotite from Sopcha, northern Russia (Kazakov, 1965), the Castle rock from a lherzolite nodule in basalts from British Columbia, Canada (Littlejohn and Greenwood, 1974), a majorite-bearing peridotite from Western Gneiss Region, Norway (Katayama et al., 2005), Zhimafang garnet peridotite from the southern Sulu, China (Xu et al., 2005), some deep sheared lherzolite xenoliths from kimberlite magmas (Lori Kennedy, private communication 2001), and other peridotites studied by the following authors (e.g., Mercier, 1977; Krull and Voll, 1978; Cordellier et al., 1981; Shuguang and Li, 1998; Tommasi et al., 2000; Pennock et al., 2003; Mehl et al., 2003). Our experimental data provide the first data set to interpret these fabrics in terms of physical and chemical (water content) conditions. In doing so, the scaling issues need to be considered. The current results (summarized in Fig. 9) can be applied directly to deformation at high temperatures ($T/T_m \sim 0.7$, i.e., asthenospheric conditions), whereas these results need to be modified if they are applied to lower temperatures. Katayama and Karato (submitted for publication) investigated the temperature effects on olivine fabrics and showed that the boundary between type-B and type-C fabric is sensitive to temperature as well as stress.

One important conclusion from these studies (see also Katayama et al., 2004; Skemer et al., submitted for publication) is that the olivine fabrics other than type-A are found mostly from convergent boundaries or from deep continental upper mantle. However, even in deep continental upper mantle (e.g., sheared lherzolites that are likely deformed at ~ 150–200 km depth) show type-A fabric in most cases (Jin, 1995; Skemer et al., submitted for publication). Therefore, we conclude that a majority of the continental lithosphere is water-poor, whereas some very deep continental lithosphere and some regions of the subduction zone upper mantle contain a large amount of water.

Seismic anisotropy in the upper mantle has been usually interpreted using the type-A fabric (Nicolas and Christensen, 1987; Silver, 1996; Smith et al., 2001). However, observed anisotropy in collision zones and in regions including hot-spots are difficult to interpret by the type-A fabrics (Jung and Karato, 2001b; Karato, 2003). Our results suggest that the seismic signatures of type-B or type-C or type-E fabric are distinct from those of type-A fabric.

According to petrological studies, the water content in the source region of mid-ocean ridge basalt (MORB) (i.e., the oceanic asthenosphere) contains ~ 500–1000 ppm H/Si (e.g., Hirth and Kohlstedt, 1996). According to the fabric diagram appropriate for asthenospheric temperatures (i.e., Fig. 9), the dominant olivine fabric there will be either type-E or type-C dependent on the water content. Similarly, water contents in basalts from hotspots are systematically larger than those in MORB (e.g., Wallace, 1998; Jamtveit et al., 2001). Therefore anomalous seismic anisotropy beneath hotspots reported by Montagner and Guillot (2000) and Gaherty (2001) may partly be due to high water contents (see also Jung and Karato, 2001b; Karato, 2003).

The pattern of shear wave splitting is complicated in the subduction zone. In many subduction zones, the polarization of the fast shear wave near a trench is often parallel to the trench (Ando et al., 1983; Shih et al., 1991; Iidaka and Obara, 1995; Yang and Fischer, 1995; Fouch and Fischer, 1996; Margheriti et al., 1996; Smith et al., 2001; Christensen et al., 2003; Shimizu et al., 2003; Nakajima and Hasegawa, 2004; Long and van der Hilst, 2005). This phenomenon can be explained by the water-rich fabrics such as the type-B LPO (Jung and Karato, 2001b). It is also observed that the polarization of fast shear wave becomes normal to the trench far way from the trench (e.g., Smith et al., 2001; Nakajima and Hasegawa, 2004; Long and van der Hilst, 2005). A plausible model to explain such an observation is to invoke a change in olivine fabric from type-B near the trench to type-A (or type-E or type-C) away from trench due to the variation in temperature and/or water content (Karato, 2003; Kneller et al., 2005).

5. Summary and concluding remarks

We have found that water has a dramatic effect on the LPO of olivine. Three new types of LPO (called type-B, C, and E) of olivine have been found (Figs. 7, 9, and 10)). Our laboratory results have reproduced most of the LPOs of olivine found in naturally deformed peridotites. We note that some of the LPOs of olivine in naturally deformed peridotites and some seismological observations could well be attributed to these new types of LPOs.

However, some fundamental issues remain unresolved including the precise scaling laws that are needed when the present results are to be applied to different conditions. Particularly important is the influence of temperature. A simple scaling analysis suggests that some of the fabric transitions are sensitive to temperature (Karato (in press). Katayama and Karato (submitted for publication) investigated that the transition between type-B and type-C fabric is sensitive to temperature and stress. Therefore, it is essential to extend the present work including the temperature effect explicitly to obtain a fabric diagram into three-dimensional space. The exact atomistic mechanisms for the observed fabric transitions

are not well constrained. A TEM study is underway to obtain better constraints on the cause for the change in the dominant slip systems (e.g., Sharp et al., 2003). Katayama and Karato (in preparation) also explore the influence of water on Peierls stress in olivine that may have a clue as to the cause for fabric transitions.

Finally, we have focused on "steady-state" fabrics in this study. Obviously non-steady-state fabric could occur in nature, and the time scale to modify the pre-existing fabrics is an important issue particularly in regions where dominant fabric types are expected to change spatially (e.g., subduction zones; Kaminski and Ribe, 2002). We have relatively limited experimental data to provide any detailed comment on this topic. However, we may mention that the kinetics of development of LPO depends highly on the water content, temperature and stress and a more extensive study will be needed to address this issue.

Our experimental studies have shown that the relationship between deformation geometry and seismic anisotropy in the upper mantle can be changed with the physical and chemical conditions of deformation. This implies that even for a simple geometry of flow, one might expect to see a complicated variation in seismic anisotropy. Consequently, sophisticated seismological techniques will be required to map the detailed pattern of seismic anisotropy in the Earth to obtain geodynamically important information from seismic anisotropy (e.g., Long et al., 2005).

Acknowledgements

This research was supported by the grant from NSF (EAR-9903087, EAR-0001955, and EAR-0309448). H. Jung was partially supported by both the University of Minnesota Doctoral Dissertation Fellowship and the BK21 at Seoul National University. T. Hiraga was funded by a JSPS Postdoctoral Fellowship for Research Abroad. We also thank Y. Zhou, Z. C. Wang, K. H. Lee, M. Zimmerman, D. Yamazaki, Y. Xu, T. Shimmei, J. Lawlis, P. Skemer, S. Mei, Z. Wang, D. Mainprice, M. M. Hirschmann, M. Bystricky, D. L. Kohlstedt and H. W. Green for their help and discussions.

References

Ando, M., Ishikawa, Y., Yamazaki, F., 1983. Shear wave polarization anisotropy in the upper mantle beneath Honshu, Japan. J. Geophys. Res. 88, 5850–5864.

Abramson, E.H., Brown, J.M., Slutsky, L.J., Zaug, J., 1997. The elastic constants of San Carlos Olivine to 17 GPa. J. Geophys. Res., B 102 (6), 12253–12263.

Avé Lallemant, H.G., Carter, N.L., 1970. Syntectonic recrystallization of olivine and modes of flow in the upper mantle. Geol. Soc. Am. Bull. 81, 2203–2220.

Bell, D.R., Rossman, G.R., 1992. Water in Earth's mantle: the role of nominally anhydrous minerals. Science 255, 1391–1397.

Bell, D.R., Rossman, G.R., Maldener, A., Endisch, D., Rauch, F., 2003. Hydroxide in olivine: a quantitative determination of the absolute amount and calibration of the IR spectrum. J. Geophys. Res. 108, 2105, doi:10.1029/2001JB000679.

Ben Ismail, W., Mainprice, D., 1998. An olivine fabric database: an overview of upper mantle fabrics and seismic anisotropy. Tectonophysics 296, 145–158.

Buiskool Toxopeus, J.M.A., 1976. Petrofabrics, microtextures and dislocation substructures of olivine in a peridotite mylonite (Alpe Arami, Switzerland). Leidse Geol. Meded. 51 (1), 1–36.

Buiskool Toxopeus, J.M.A., 1977. Fabric development of olivine in a peridotite mylonite. Tectonophysics 39, 55–71.

Bunge, H.J., 1982. Texture Analysis in Material Sciences. Butterworths, London, p. 593.

Bystricky, M., Kunze, K., Burlini, L., Burg, J.-P., 2000. High shear strain of olivine aggregates: rheological and seismic consequences. Science 290, 1564–1567.

Carter, N.L., Avé Lallemant, H.G., 1970. High temperature flow of dunite and peridotite. Geol. Soc. Am. Bull. 81, 2181–2202.

Chopra, P.N., Paterson, M.S., 1981. The experimental deformation of dunite. Tectonophysics 78, 453–473.

Chopra, P.N., Paterson, M.S., 1984. The role of water in the deformation of dunite. J. Geophys. Res. 86, 7861–7876.

Christensen, D.H., Abers, G.A., McKnight, T.L., 2003. Mantle anisotropy beneath the Alaska range inferred from S-wave splitting observations: results from BEAAR. Eos. Trans. AGU 84 (46) (Fall Meet. Suppl., Abstract, F1052).

Cordellier, F., Boudier, F., Boullier, A.M., 1981. Structural study of the Almklovdalen peridotite massif (Southern Norway). Tectonophysics 77, 257–281.

Couvy, H., Frost, D., Heidelbach, F., Nyilas, K., Ungar, T., Mackwell, S.J., Cordier, P., 2004. Shear deformation experiments of forsterite at 11 GPa–1400 °C in the multianvil apparatus. Eur. J. Mineral. 16, 877–889.

Dingley, D.J., 1984. Diffraction from sub-micron areas using electron backscattering in a scanning electron microscope. Scanning Electron Microsc. 2, 569–575.

Dingley, D.J., Randle, V., 1992. Review — microstructure determination by electron back-scatter diffraction. J. Mater. Sci. 27, 4545–4566.

Fouch, M.J., Fischer, K.M., 1996. Mantle anisotropy beneath northwest Pacific subduction zones. J. Geophys. Res. 101, 15987–16002.

Frese, K., Trommsdorf, V., Wenk, H.-R., Kunze, K., 2001. Deform. Mech. Rheol. Tectonics 53, 54.

Frese, K., Trommsdorff, V., Kunze, K., 2003. Olivine [100] normal to foliation: lattice-preferred orientation in prograde garnet peridotite formed at high H_2O activity, Cima di Gagnone (Central Alps). Contrib. Mineral. Petrol. 145, 75–86.

Gaherty, J.B., 2001. Seismic evidence for hotspot-induced buoyant flow beneath the Reykjanes ridge. Science 293, 1645–1647.

Getting, I.C., Kennedy, G.C., 1970. Effect of pressure on the emf of chromel–alumel and platinum–platinum 10% rhodium thermocouples. J. Appl. Phys. 41 (11), 4552–4562.

Gifkins, R.C., 1970. Optical microscopy of metals. Elsevier, New York.

Girimmer, H., 1979. Distribution of disorientation angles if all relative orientations of neighboring grains are equally probable. Scr. Metall. 13 (2), 161–164.

Gleason, G.C., Tullis, J., 1993. Improving flow laws and piezometers for quartz and feldspar aggregates. Geophys. Res. Lett. 20, 2111–2114.
Green, H.W., Borch, R.S., 1989. A new molten salt cell for precision stress measurement at high pressure. Eur. J. Mineral. 1, 213–219.
Heggie, M., Jones, R., 1986. Models of hydrolytic weakening in quartz. Philos. Mag., A 53 (5), L65–L70.
Hirth, G., Kohlstedt, D.L., 1996. Water in the oceanic upper mantle: implications for rheology, melt extraction and the evolution of the lithosphere. Earth Planet. Sci. Lett. 144, 93–108.
Holtzman, B., Kohlstedt, D.L., Zimmerman, M.E., Heidelbach, F., Hiraga, T., Hustoft, J., 2003. Melt segregation and strain partitioning: implications for seismic anisotropy and mantle flow. Science 301, 1227–1230.
Iidaka, T., Obara, K., 1995. Shear-wave polarization anisotropy in the mantle wedge above the subducting Pacific plate. Tectonophysics 249, 53–68.
Jamtveit, B., Brooker, R., Brooks, K., Larsen, L.M., Pedersen, T., 2001. The water content of olivines from the north Atlantic volcanic province. Earth Planet. Sci. Lett. 186, 401–415.
Jin, D., 1995. Deformation microstructures of some ultramafic rocks. MSc. Thesis, University of Minnesota, pp. 115.
Jung, H., 2002. Effects of water on the plastic deformation and deformation microstructure of olivine. Ph. D. Thesis, University of Minnesota, Minneapolis, pp. 147.
Jung, H., Karato, S., 2001a. Effects of water on dynamically recrystallized grain-size of olivine. J. Struct. Geol. 23, 1337–1344.
Jung, H., Karato, S., 2001b. Water-induced fabric transitions in olivine. Science 293, 1460–1463.
Kaminski, E., Ribe, N.M., 2002. Timescales for the evolution of seismic anisotropy in mantle flow. Geochem. Geophys. Geosyst. 3 (8), doi:10.1029/2001GC000222.
Karato, S., 1987a. Seismic anisotropy due to lattice-preferred orientation of minerals: kinematic or dynamic? In: Manghnani, M.H., Syono, Y. (Eds.), High Pressure Research in Geophysics. Geophysical Monograph, vol. 39. Amer. Geophys. Union, Washington, D. C., pp. 455–471.
Karato, S., 1987b. Scanning electron microscope observation of dislocations in olivine. Phys. Chem. Miner. 14, 245–248.
Karato, S., 1989. Grain growth kinetics in olivine aggregates. Tectonophysics 168, 255–273.
Karato, S., 1995. Effects of water on seismic wave velocities in the upper mantle. Proc. Jpn. Acad. 71 (Ser. B), 61–66.
Karato, S., 2003. Mapping water content in the upper mantle. In: Eiler, J. (Ed.), Inside the Subduction Factory. AGU Monograph, Washington, DC, vol. 138, pp. 135–152.
Karato, S., in press. Microscopic models for the influence of hydrogen on the physical and chemical properties of minerals, In "Super plume: beyond plate tectonics" (eds. D.A. Yuen, S. Maruyama, S. Karato and B.F. Windley), Springer Verlag, New York.
Karato, S., Jung, H., 2003. Effects of pressure on high-temperature dislocation creep in olivine. Philos. Mag., A 83 (3), 401–414.
Karato, S., Lee, K.-H., 1999. Stress and strain distribution in deformed olivine aggregates: inference from microstructural observations and implications for texture development. In: Szpunar, J.A. (Ed.), Proceedings of the twelfth international conference on textures of materials. ITOCOM-12, vol. 2, pp. 1546–1555.
Karato, S., Paterson, M.S., Fitz Gerald, J.D., 1986. Rheology of synthetic olivine aggregates: influence of water and grain size. J. Geophys. Res. 91, 8151–8176.
Katayama, I., Karato, S., submitted for publication. Effect of temperature on the B- to C-type olivine fabric transition and implication for flow pattern in the subduction zone. Earth Planet. Sci. Letts.
Katayama, I., Karato, S., in preparation. Effect of water on low temperature, high stress rheology of olivine.
Katayama, I., Jung, H., Karato, S., 2004. A new type of olivine fabric at modest water content and low stress. Geology 32 (12), 1045–1048.
Katayama, I., Karato, S., Brandon, M., 2005. Evidence of high water content in the deep upper mantle inferred from deformation microstructures. Geology 33 (7), 613–616.
Kazakov, A.N., 1965. Microstructural orientation of olivine in rocks of the supposed upper earth mantle. Zap. Vsesoyuzn. Min. Obshch. 94, 576–580.
Kneller, E.A., van Keken, P.E., Karato, S.I., Park, J., 2005. B-type olivine fabric in the mantle wedge: insight from high-resolution non-Newtonian subduction zone models. Earth Planet. Sci. Lett. 237, 781–797.
Kohlstedt, D.L., Goetze, C., Durham, W.B., 1976a. Experimental deformation of single crystal olivine with application to flow in the mantle. In: Strens, R.G.J. (Ed.), The Physics and Chemistry of Minerals and Rocks. John Wiley & Sons, pp. 35–49.
Kohlstedt, D.L., Goetze, C., Durham, W.B., Vander Sande, J.B., 1976b. Science 191, 1045–1046.
Kohlstedt, D.L., Keppler, H., Rubie, D.C., 1996. Solubility of water in the α, β, γ phases of $(Mg,Fe)_2SiO_4$. Contrib. Mineral. Petrol. 123, 345–357.
Krull, J.H., Voll, G., 1978. Deformation and metamorphism of the western Finero Complex. From: Proceedings of the 2nd symposium Ivrea–Verbano, Varallo Sesia (VC), Italy, June 5–10, 1978. Memorie Di Scienze Geologiche, vol. XXXIII, pp. 95–109.
Lee, K.-H., Jiang, Z., Karato, S., 2002. A scanning electron microscope study of the effects of dynamic recrystallization on lattice-preferred orientation in olivine. Tectonophysics 351, 331–341.
Littlejohn, A.L., Greenwood, H.J., 1974. Lherzolite nodules in basalts from British Columbia, Canada. Can. J. Earth Sci. 11, 1288–1308.
Lloyd, G.E., 1987. Atomic number and crystallographic contrast images with the SEM: a review of backscattered techniques. Mineral. Mag. 51, 3–19.
Long, M.D., van der Hilst, R.D., 2005. Upper mantle anisotropy beneath Japan from shear wave splitting. Phys. Earth and Planet. Int. 151, 206–222.
Long, M.D., van der Hilst, R.D., de Hoop, M.V., Hager, B.H., 2005. Constraints on deformation geometry beneath Japan from observations and models of seismic anisotropy. Eos Trans. AGU 86 (52) (Fall Meet. Suppl., Abstract T31D-03).
Mackwell, S.J., Kohlstedt, D.L., Paterson, M.S., 1985. Role of water in the deformation of olivine single crystals. J. Geophys. Res. 90, 11319–11333.
Mainprice, D., 1990. A FORTRAN program to calculate seismic anisotropy from the lattice-preferred orientation of minerals. Comput. Geosci. 16, 385–393.
Mainprice, D., Silver, P.G., 1993. Interpretation of SKS-waves using samples from the subcontinental lithosphere. Phys. Earth Planet. Inter. 78, 257–280.
Mainprice, D., Barruol, G., Ben Ismail, W., 2000. The seismic anisotropy of the Earth's mantle: from single crystal to polycrystal. In: Karato, S., Forte, A., Liebermann, R., Masters, G., Stixrude, L. (Eds.), Earth's Deep Interior-Mineral physics and Tomography From the Atomic to the Global Scale. American Geophysical Union, Washington, D.C., pp. 237–264.
Margheriti, L., Nostro, C., Cocco, M., Amato, A., 1996. Seismic anisotropy beneath the Northern Apennines (Italy) and its tectonic implications. Geophys. Res. Lett. 23, 2721–2724.
McLaren, A.C., 1991. Transmission Electron Microscopy of Minerals and Rocks. Cambridge University Press, Cambridge.

Mehl, L., Hacker, B.R., Hirth, G., Kelemen, P.B., 2003. Arc-parallel flow within the mantle wedge: evidence from the accreted Talkeetna arc, south central Alaska. J. Geophys. Res. 108 (B8), 2375, doi:10.1029/2002JB002233.

Mei, S., Kohlstedt, D.L., 2000a. Influence of water on plastic deformation of olivine aggregates. 1. Diffusion creep regimes. J. Geophys. Res. 105, 21457–21469.

Mei, S., Kohlstedt, D.L., 2000b. Influence of water on plastic deformation of olivine aggregates. 2. Dislocation creep regime. J. Geophys. Res. 105, 21471–21481.

Mercier, J-C. C., 1977. Natural peridotites, chemical and rheological heterogeneity of the upper mantle. Ph. D. Thesis, State University of New York at Stony Brook.

Mercier, J.-C.C., 1985. Ch. 19: olivine and pyroxenes. In: Wenk, H.-R. (Ed.), Preferred Orientation in Deformed Metals and Rocks: an Introduction to Modern Texture Analysis. Academic Press, New York, pp. 407–430.

Miller, G.H., Rossman, G.R., Harlow, G.E., 1987. The natural occurrence of hydroxide in olivine. Phys. Chem. Miner. 14, 461–472.

Mirwald, P.W., Getting, I.C., Kennedy, G.C., 1975. Low-friction cell for piston-cylinder high-pressure apparatus. J. Geophys. Res. 80, 1519–1525.

Mizukami, T., Wallis, S., Yamamoto, J., 2004. Natural examples of olivine lattice-preferred orientation patterns with a flow-normal *a*-axis maximum. Nature 427, 432–436.

Möckel, J.R., 1969. Structural petrology of the garnet-peridotite of Alpe Arami (Ticino, Switzerland). Leidse Geol. Meded. 42, 61–130.

Montagner, J.P., Guillot, L., 2000. Seismic anisotropy in the Earth's mantle. In: Boschi, E., Ekström, G., Morelli, A. (Eds.), Problems in Geophysics for the New Millennium, pp. 217–253.

Nakajima, J., Hasegawa, A., 2004. Shear-wave polarization anisotropy and subduction-induced flow in the mantle wedge of northern Japan. Earth Planet. Sci. Lett. 225, 365–377.

Nicolas, A., 1976. Flow in upper-mantle rocks: some geophysical and geodynamic consequences. Tectonophysics 32, 93–106.

Nicolas, A., Christensen, N.I., 1987. Formation of anisotropy in upper mantle peridotites — a review. In: Fuchs, K., Froidevaux, C. (Eds.), The Composition, Structure, and Dynamics of the Lithosphere–Asthenosphere System. American Geophysical Union, Washington, D.C., pp. 111–123.

Nicolas, A., Bouchez, J.L., Boudier, F., Mercier, J.C., 1971. Textures, structures and fabrics due to solid state flow in some European lherzolites. Tectonophysics 12, 55–86.

Nicolas, A., Boudier, F., Boullier, A.M., 1973. Mechanisms of flow in naturally and experimentally deformed peridotites. Am. J. Sci. 273, 853–876.

Paterson, M.S., 1982. The determination of hydroxyl by infrared absorption in quartz, silicate glasses and similar materials. Bull. Mineral. 105, 20–29.

Pennock, G.M., Drury, M.R., Ave Lallemant, H.G., 2003. Grain size reduction and deformation mechanisms in ultra-fine-grained shear zones from the Lherz Peridotite. Eos. Trans. AGU 84 (46) (Fall Meet. Suppl., Abstract, F1422).

Prior, D.J., Boyle, A.P., Brenker, F., Cheadle, M.C., Day, A., Lopez, G., Peruzzo, L., Potts, G.J., Reddy, S., Spiess, R., Timms, N.E., Trimby, P., Wheeler, J., Zetterström, L., 1999. The application of electron backscatter diffraction and orientation contrast imaging in the SEM to textural problems in rocks. Am. Mineral. 84, 1741–1759.

Sharp, T.G., Jung, H., Fitz Gerald, J., Karato, S., 2003. Dislocation microstructures in deformed olivine displaying the C-type and B-type fabrics. Eos. Trans. AGU 84 (46) (Fall Meet. Suppl., Abstract, F1431).

Shih, X.R., Schneider, J.F., Meyer, R.P., 1991. Polarities of P and S waves, and shear wave splitting observed from the Bucaramanga Nest, Colombia. J. Geophys. Res. 96, 12069–12082.

Shimizu, J., Nakajima, J., Hasegawa, A., 2003. Shear-wave polarization anisotropy in the mantle wedge beneath the southern part of Tohoku, Japan. Eos. Trans. AGU 84 (46) (Fall Meet. Suppl., Abstract, F1052).

Shuguang, S., Li, S., 1998. Rheological properties of mantle peridotites at Yushigou in the north Qilian Mountain and their implications for plate dynamics. Acta Geol. Sin. 72, 131–141.

Silver, P., 1996. Seismic anisotropy beneath the continents: probing the depths of geology. Annu. Rev. Earth Planet. Sci. 24, 385–432.

Skemer, P., Katayama, I., Jiang, Z., Karato, S., 2005. The misorientation index: development of a new method for calculating the strength of lattice-preferred orientation. Tectonophysics 411, 157–167.

Skemer, P., Katayama, I., Karato, S., submitted for publication. Deformation fabrics of the Cima di Gagnone Peridotite Massif, Central Alps, Switzerland: evidence of deformation under water-rich conditions at low temperatures, Submitted to Contributions to Mineralogy and Petrology.

Smith, G.P., Wiens, D.A., Fisher, K.M., Dorman, L.M., Webb, S.C., Hildebrand, J.A., 2001. A complex pattern of mantle flow in the Lau backarc. Science 292, 713–716.

Tommasi, A., Mainprice, D., Canova, G., Chastel, Y., 2000. Viscoplastic self-consistent and equilibrium-based modeling of olivine lattice-preferred orientations: implications for the upper mantle seismic anisotropy. J. Geophys. Res. 105, 7893–7908.

van Houte, P., Wagner, F., 1985. Development of texture by slip and twinning. In: Wenk, H.-R. (Ed.), Preferred Orientation in Deformed Metals and Rocks: Introduction to Modern Texture Analysis. Academic Press, San Diego, pp. 233–258.

Wallace, P.J., 1998. Water and partial melting in mantle plumes: inferences from the dissolved H_2O concentrations of Hawaiian basaltic magmas. Geophys. Res. Lett. 25, 3639–3642.

Wenk, H.R., 2002. Texture and anisotropy. In: Karato, S.I., Wenk, H. R. (Eds.), Plastic Deformation of Minerals and Rocks. Reviews in Minerology and Geochemistry, vol. 51, pp. 291–329.

Xu, Z.Q., Chen, J., Wang, Q., Zeng, L.S., Yang, J.S., Chen, F.Y., Liang, F.H., 2005. Type-C olivine fabric in the Zhimafang garnet peridotite of the southern Sulu ultrahigh-pressure metamorphic terrane: formation conditions and tectonic implications. Acta Petrol. Sin. 21 (2), 389–397.

Yang, X., Fischer, K.M., 1995. Seismic anisotropy beneath the Shumagin Islands segment of the Aleutian–Alaska subduction zone. J. Geophys. Res. 100, 18165–18177.

Yoshino, G., 1961. Structural–petrological studies of peridotite and associated rocks of the Higashi-akaishi-yama District, Shikoku. Japan. J. Sci. Hiroshima Univ., Ser. C 3, 343–402.

Zhang, S., Karato, S., 1995. Lattice-preferred orientation of olivine aggregates in simple shear. Nature 375, 774–777.

Zhang, S., Karato, S., Fitz Gerald, J.D., Faul, U.H., Zhou, Y., 2000. Simple shear deformation of olivine aggregates. Tectonophysics 316, 133–152.

Zimmerman, M.E., Zhang, S., Kohlstedt, D.L., Karato, S., 1999. Melt distribution in mantle rocks deformed in shear. Geophys. Res. Lett. 26, 1505–1508.